A DNM2 centronuclear myopathy mutation reveals a link between recycling endosome scission and autophagy

Claudia Puri, Marco M Manni, Mariella Vicinanza, Christine Hilcenko, Ye Zhu, Gautam Runwal, Eleanna Stamatakou, Fiona M Menzies, Kamel Mamchaoui, Marc Bitoun, et al.

Article

Developmental Cell

A DNM2 Centronuclear Myopathy Mutation Reveals a Link between Recycling Endosome Scission and Autophagy

Graphical Abstract

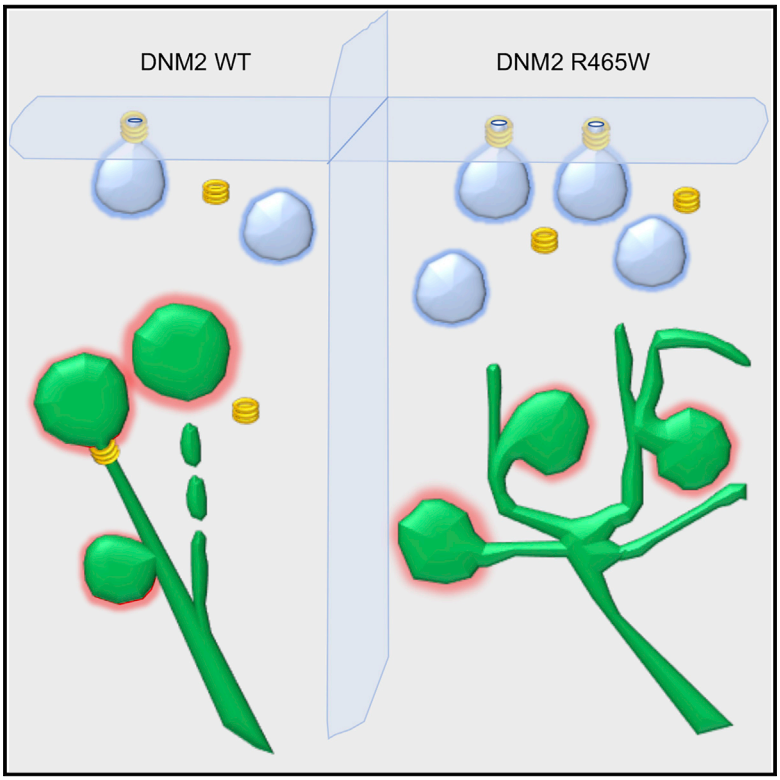

Authors

Claudia Puri, Marco M. Manni, Mariella Vicinanza, ..., Kamel Mamchaoui, Marc Bitoun, David C. Rubinsztein

Correspondence

dcr1000@cam.ac.uk

In Brief

Puri et al. show that autophagosome release from recycling endosomes requires DNM2-dependent scission. This process is enabled by DNM2 binding the core autophagy protein LC3 and is impaired by a DNM2 centronuclear myopathy mutant that is sequestered away from autophagosome formation sites by enhanced binding to plasma membrane ITSN1.

Highlights

- Autophagosome release from recycling endosomes requires DNM2-dependent scission
- Recycling endosome scission is regulated by DNM2 binding to LC3
- Recycling endosome scission is impaired by a DNM2 centronuclear myopathy mutant
- This DNM2 mutant is sequestered from autophagosome formation sites by binding ITSN1

Puri et al., 2020, Developmental Cell *53*, 154–168
April 20, 2020
https://doi.org/10.1016/j.devcel.2020.03.018

CellPress

CellPress

Developmental Cell
Article

A DNM2 Centronuclear Myopathy Mutation Reveals a Link between Recycling Endosome Scission and Autophagy

Claudia Puri,[1,2,3] Marco M. Manni,[1,2] Mariella Vicinanza,[1,2,3] Christine Hilcenko,[2,4,5] Ye Zhu,[1,2] Gautam Runwal,[1,2] Eleanna Stamatakou,[1,2,3] Fiona M. Menzies,[1,2] Kamel Mamchaoui,[6] Marc Bitoun,[6] and David C. Rubinsztein[1,2,3,7,*]

[1]Department of Medical Genetics, Cambridge Biomedical Campus, Hills Road, Cambridge CB2 0XY, UK
[2]Cambridge Institute for Medical Research, The Keith Peters Building, Cambridge Biomedical Campus, Hills Road, Cambridge CB2 0XY, UK
[3]UK Dementia Research Institute, Cambridge BioMedical Campus, The Keith Peters Building, Hills Road, Cambridge CB2 0XY, UK
[4]Department of Haematology, University of Cambridge, Cambridge CB2 0XY, UK
[5]Wellcome Trust–Medical Research Council Stem Cell Institute, University of Cambridge, Jeffrey Cheah Biomedical Centre Puddicombe Way, Cambridge Biomedical Campus, Cambridge CB2 0AW, UK
[6]Myology Center for Research, U974, Sorbonne Université - INSERM - American Institute of Mathematics, GH Pitie Salpetrière, Paris 75013, France
[7]Lead Contact
*Correspondence: dcr1000@cam.ac.uk
https://doi.org/10.1016/j.devcel.2020.03.018

SUMMARY

Autophagy involves engulfment of cytoplasmic contents by double-membraned autophagosomes, which ultimately fuse with lysosomes to enable degradation of their substrates. We recently proposed that the tubular-vesicular recycling endosome membranes were a core platform on which the critical early events of autophagosome formation occurred, including LC3-membrane conjugation to autophagic precursors. Here, we report that the release of autophagosome precursors from recycling endosomes is mediated by DNM2-dependent scission of these tubules. This process is regulated by DNM2 binding to LC3 and is increased by autophagy-inducing stimuli. This scission is defective in cells expressing a centronuclear-myopathy-causing DNM2 mutant. This mutant has an unusual mechanism as it depletes normal-functioning DNM2 from autophagosome formation sites on recycling endosomes by causing increased binding to an alternative plasma membrane partner, ITSN1. This "scission" step is, thus, critical for autophagosome formation, is defective in a human disease, and influences the way we consider how autophagosomes are formed.

INTRODUCTION

Macroautophagy (henceforth autophagy) is the process where cells engulf cytoplasmic contents in double-membraned autophagosomes, which traffic their contents to lysosomes for degradation (Fass et al., 2006). This pathway, which is conserved from yeast to humans, helps maintain cellular homeostasis by degrading substrates including protein complexes, aggregate-prone proteins (e.g., in neurodegenerative diseases), various pathogens, and dysfunctional organelles (like mitochondria and peroxisomes) (Eskelinen, 2019; Menzies et al., 2017). Accordingly, autophagy impacts many human diseases, including forms of neurodegeneration, cancer, infections, and inflammation (Hansen et al., 2018; Tang et al., 2019).

A key question is how do cells generate these vesicles that have double membranes? The precursors of autophagosomes are cup-shaped double-membrane structures called phagophores. These originate from membranes where key events occur, including PI(3)P (phosphatidylinositol 3-phosphate) synthesis mediated by an enzyme complex including Beclin 1 and the PI 3-kinase VPS34, which leads to the PI(3)P-dependent recruitment of WIPI2, which then recruits the ATG5-12/ATG16L1 complex that enables the conjugation of ATG8 family members (like LC3s) to the nascent phagophore membranes. This ubiquitin-like conjugation of ATG8 members to autophagosomes represents a defining step in autophagosome formation (Dooley et al., 2014; Vicinanza et al., 2015).

Many different membranes have been proposed to contribute to autophagosomes, including the plasma membrane, endosomes, various domains of the ER (endoplasmic reticulum), and the Golgi apparatus (Axe et al., 2008; Hamasaki et al., 2013; Hayashi-Nishino et al., 2009; Knævelsrud et al., 2013a; Longatti et al., 2012; Puri et al., 2013, 2018a; Ravikumar et al., 2010; Shibutani and Yoshimori, 2014; Ylä-Anttila et al., 2009). We recently proposed that the recycling endosome RAB11A-positive membranes were a core platform on which the critical early events of autophagosome formation occurred leading up to LC3 conjugation—the recruitment of WIPI2 and subsequent autophagosome formation was not only dependent on PI(3)P (which is also found in membranes that are known not to directly form autophagosomes) but also required WIPI2 binding to RAB11A (Puri et al., 2018a). Our previous data suggested that most, if not all, autophagosomes had this RAB11A-dependency for their formation—for instance, WIPI2 knockdown cells reconstituted with mutant forms of WIPI2 that could not bind RAB11A had almost complete abrogation of WIPI2- or ATG16L1-positive autophagosome precursors, compared with those reconstituted

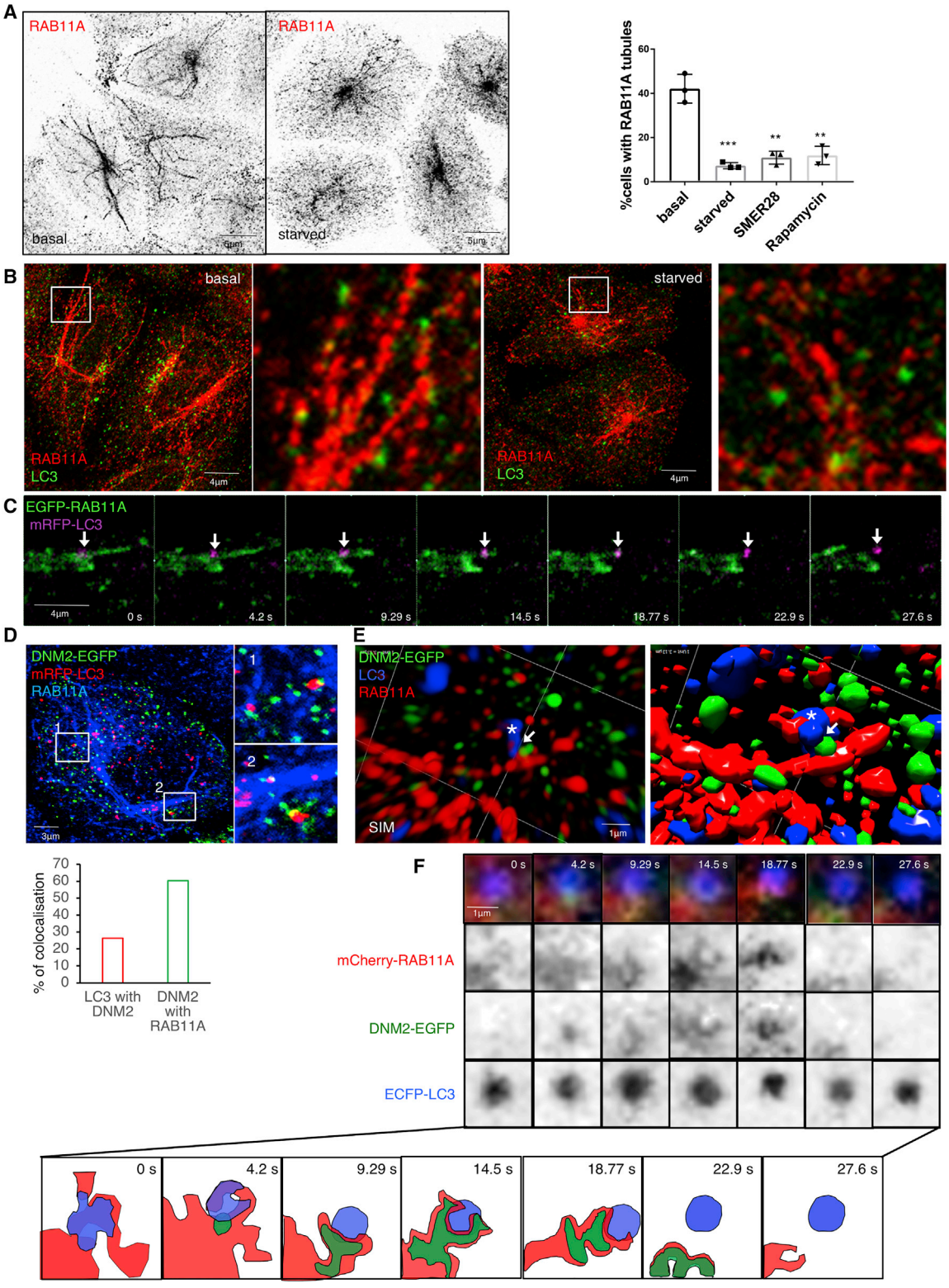

Figure 1. Recycling Endosomes Fragment to Release Autophagosomes

(A) HeLa cells were fixed in basal conditions or after overnight treatment with Hank's balanced salt solution (HBSS) (starved) and stained with RAB11A antibody. Histogram shows quantification of the percentage of cells showing RAB11A tubules in HeLa cells treated overnight with HBSS (starved), rapamycin, or SMER28. Data are mean ± SD, (n = 3; graphs represent means of the triplicates from three independent experiments); two-tailed paired t test, $^{**}p < 0.01$, $^{***}p < 0.001$.

(B) HeLa cells were fixed in basal conditions or after 4 h of starvation in HBSS and labeled for RAB11A and LC3.

(legend continued on next page)

with wild-type (WT) WIPI2 (Puri et al., 2018a). Furthermore, WIPI2 knockdown cells reconstituted with mutant forms of WIPI2 that could not bind RAB11A had increased levels of autophagy substrate accumulation (mutant huntingtin aggregation) similar to WIPI2 knockdown cells, while those cells reconstituted with WT WIPI2 had much lower levels (~50%) of these substrates, similar to control cells. The RAB11A structures that acquired LC3 were considered to be autophagosomes as they had double membranes and engulfed autophagic substrates like p62, mutant huntingtin, and mitochondria (Puri et al., 2018a). Our data are compatible with other recent studies that link autophagy and the recycling endosome (Izumi et al., 2019; Longatti et al., 2012; Puri et al., 2013; Søreng et al., 2018).

If the key molecular events leading to and including LC3 conjugation to nascent autophagosome membranes occur on tubular-vesicular recycling endosome membranes, this can explain how autophagosomes have double membranes and why endocytosed transferrin and the extracellular domain of the transferrin receptor are found between the inner and outer membranes of phagophores and autophagosomes (Longatti et al., 2012; Puri et al., 2018a). This phenomenon is consistent with the membrane topology that would arise if the two membranes of autophagosomes formed from recycling endosome tubules (Puri et al., 2018b). However, this model requires a step of recycling endosome tubule scission to release nascent phagophores, a step in autophagosome formation that has previously not been described.

An important mediator of tubulated membrane scission in other cellular contexts is dynamin 2 (DNM2), a ubiquitously expressed large GTPase (Ferguson and De Camilli, 2012). DNM2 comprises five domains: an N-terminal GTPase domain, followed by the middle and pleckstrin-homology (PH) domains, the GTPase effector domain (GED), and the C-terminal proline-arginine-rich domain (PRD). DNM2 mutations cause autosomal dominant centronuclear myopathy (CNM), a condition that manifests with muscle weakness and wasting (Hohendahl et al., 2016; Zhao et al., 2018). Mutations affecting the middle domain (MD) are generally associated with a relatively mild clinical course, while those in the PH and GED domains are more severe (Catteruccia et al., 2013). One of the best characterized CNM mutations in DNM2 is R465W in the MD (Buono et al., 2018; Durieux et al., 2010, 2012). Fibroblasts from DNM2 R645W heterozygous (HET) mice have defective autophagy with an accumulation of immature autophagic structures (Durieux et al., 2012). Our data explain this phenotype, reveal a new step where autophagy can be blocked in disease, and characterize the mechanism, since the DNM2 R465W mutation reveals an unforeseen link between recycling endosome scission and autophagy.

RESULTS

Recycling Endosomes Fragment to Release Nascent Autophagosomes

When autophagy is induced with mTOR-dependent or -independent stimuli, the recycling endosome RAB11A-positive tubules fragment and LC3-positive structures are released from this compartment (Figures 1A–1C; Video S1). We tested if DNM2 mediated this process, as cells with the DNM2 R465W mutation that causes autosomal dominant centronuclear myopathy manifest an accumulation of immature autophagic structures (Durieux et al., 2012). DNM2 detaches endocytic vesicles from the plasma membrane (Ferguson and De Camilli, 2012; Sundborger and Hinshaw, 2014) but is also present on recycling endosomes (Søreng et al., 2018; van Dam and Stoorvogel, 2002). We isolated recycling endosomes by magnetic isolation after chasing iron microbeads conjugated to transferrin-Alexa Fluor 488 into this compartment (Puri et al., 2018a). Using this approach, we confirmed the presence of DNM2 on recycling endosomes along with RAB11A and LC3 (Figure S1A). Interestingly the DNM2 plasma membrane binding partner, ITSN1 (intersectin-1), was not seen in the recycling endosomes fraction but only on the "unbound" fraction (Figure S1A). DNM2 colocalized with RAB11A in LC3-positive structures by confocal and superresolution structured illumination (SIM) microscopy (Figures 1D and 1E). Live imaging suggested that LC3 is present on the RAB11A compartment before DNM2, which appears to localize at the junction of LC3 and RAB11A (Figure 1F). Later in the video, DNM2 looked like it enwrapped both LC3 and RAB11A-labeled structures before autophagosome release from the recycling endosome (Figures 1F and S1B; Video S2).

LC3 Directly Interacts with DNM2

LC3-I becomes LC3-II, which has characteristic gel mobility, after it is conjugated to autophagic precursor membranes (Kabeya et al., 2000). DNM2 RNAi silencing led to LC3-II accumulation in nutrient replete (Figures 2A and S2A) or in starvation (Figure S2B) conditions but not when cells were treated with the lysosomal inhibitor, bafilomycin A1, which blocks LC3-II-autophagosome degradation, suggesting that DNM2 regulates a step in autophagy downstream of LC3 conjugation to nascent autophagosome membranes. DNM2 knockdown also caused an increase of cells with RAB11A tubules (Figure 2B), which would result from impaired recycling endosome fragmentation and increased colocalization of LC3-positive structures with the RAB11A compartment (Figures 2C and 2D). These data support a role for DNM2 in recycling endosome fragmentation

In (A) left hand panel we have 3 cells that we scored as having tubules, while the cells in the right hand panel of Figure 1A were not considered to have this tubulation state.

(C) HeLa cells were transfected for 24 h with pEGFP-RAB11A and mRFP-LC3 and processed for live imaging in HEPES-HBSS medium (see also Video S1).

(D) HeLa cells were transfected for 24 h with DNM2-pEGFP and mRFP-LC3, fixed in basal conditions and labeled for endogenous RAB11A. Histogram below shows quantification of the association of LC3 with DNM2 or DNM2 with RAB11A

(E) HeLa cells were transfected for 24 h with DNM2-pEGFP and were fixed in basal conditions and labeled for endogenous LC3 and RAB11A and processed for superresolution microscopy (SIM-Elyra). Left panel shows the structured illumination image, while right panel shows the isosurface rendering in which there is no transparency, and colocalized pixels do not appear as yellow.

(F) HeLa cells were transfected for 24 h with mCherry-RAB11A, DNM2-pEGFP, and pECFP-LC3 and processed for live imaging in 4-(2-hydroxyethyl)-1-piperazineethanesulfonic acid (HEPES)-HBSS medium.

The schematic diagram in the bottom shows outlines of the different channels in the different frames (see also Figure S1B; Video S2).

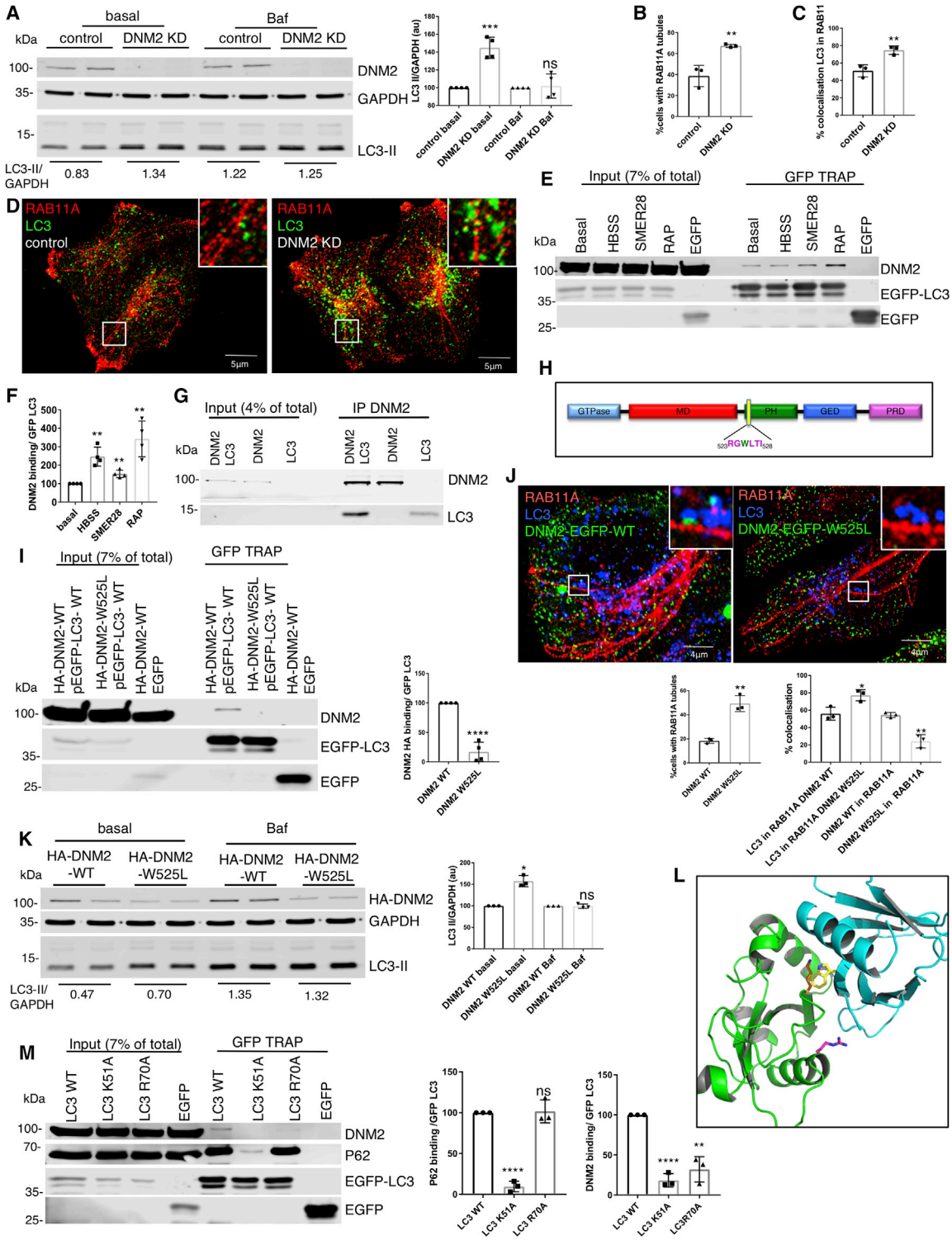

Figure 2. LC3 Directly Interacts with DNM2

(A) HeLa cells transfected with control or DNM2 siRNA oligos (mix of oligos A and B) for 3 days, treated with DMSO (basal) or bafilomycin A1 (Baf) for 4 h, processed for immunoblot and labeled for LC3, DNM2, and GAPDH as loading control. Histogram shows the relative amount of LC3-II in basal or under Baf treatment, normalized for GAPDH. Data are mean ± SD (n = 3; graphs represent means of the triplicates from three independent experiments) two-tailed paired t test, ***p < 0.001, ns, not significant. The numbers indicate the LC3-II/GAPDH value of the shown experiment.

(B–D) HeLa cells transfected with control or DNM2 siRNA oligos (mix of oligos A and B) for 3 days, fixed and labeled for endogenous LC3 and RAB11A. The histogram in (B) shows the percentage of cells with RAB11A tubules; the histogram (C) shows the quantification of the association of LC3 with RAB11A (Manders'

(legend continued on next page)

to enable the release of LC3-positive structures (phagophores/autophagosomes).

We considered that DNM2 binding to recycling endosomes may be LC3 dependent. Endogenous LC3 (Figure S2C) or GFP-tagged exogenous LC3 can bind DNM2, and the binding increases when the cells are treated with different autophagy inducers (starvation-HBSS, rapamycin, and SMER28) (Figures 2E, 2F, and S2C). As *in vitro* experiments confirmed that the LC3-DNM2 interaction was direct (Figure 2G), we searched for a potential LC3-interacting region (LIR) motif in DNM2 (Figure 2H). Mutagenesis experiments suggested that amino acids 523–528 were critical, as mutation of tryptophan 525 abolished the DNM2-LC3 interaction (Figure 2I). The protein carrying this mutation is still functional, since it still binds its plasma membrane interactor ITSN1 (Figure S2D). DNM2 knockdown cells were reconstituted with either WT or LIR-mutant (W525L) DNM2, and we observed that the LIR-mutant-expressing cells had a phenotype similar to what we observed in DNM2-depleted cells (Figures 2A–2D): an increase of cells with RAB11A tubules, an increased colocalization of LC3-positive structures with the RAB11A compartment, decreased DNM2 colocalization with RAB11A (Figure 2J), and LC3-II accumulation in nutrient replete (Figure 2K) or starvation conditions (Figure S2E) in the absence but not in the presence of bafilomycin A1. DNM2 WT re-expression in DNM2-depleted cells normalized the LC3 elevation caused by DNM2 depletion, which was not seen with the DNM2 W525L mutant (Figure S2F). Interestingly, stable overexpression of this DNM2-LIR mutant without knockdown in starved cells phenocopied the LC3-II elevation in the absence of bafilomycin, and no change in the presence of bafilomycin was seen in DNM2-knockdown cells reconstituted with the mutant (Figures S2E and S2G). Thus, this mutant likely acts as a dominant negative, as DNM2 works as an oligomer (Ross et al., 2011).

We modeled the DNM2-LC3 interaction using PyMOL software (http://www.pymol.org) (Figure 2L) to find the LC3 domain important for DNM2 interaction. We tested mutations in two different amino acids, K51 and R70 that help form a putative DNM2-binding pocket. K51 is known to be responsible for the autophagy adaptor SQSTM1/P62 interaction (Chino et al., 2019; Tung et al., 2010). The LC3 K51A mutation affects LC3 interactions with both P62 and DNM2, but LC3 R70A affects only the LC3-DNM2 interaction (Figure 2M).

Consistent with our hypothesis that LC3 recruits DNM2 to the recycling endosome to enable scission and LC3/autophagosome release, the LC3 R70A mutant localized more on RAB11A compartment than the WT, and the LC3 R70A dots on RAB11A did not associate with DNM2, while the WT LC3 clearly associated with DNM2 (Figure S3A). K51 and R70 are conserved in other ATG8 family members (Figure S3B) and DNM2 also binds other ATG8 members, like GABARAP, GABARAP-L1, and GABARAP-L2 (Figures S3B and S3C).

LC3 conjugation to phosphatidylethanolamine to form LC3-II is mediated by the E2-like enzyme ATG3 and then the E3-like ATG16L1-ATG5-ATG12 complex (Gao et al., 2013). Since DNM2 can still bind LC3 in ATG3-null cells, DNM2 can bind non-lipidated LC3 (Figure S3D). (P62 can also bind non-lipidated LC3 [Figure S3D]).

DNM2 is GTPase protein. GTPase proteins cycle between the cytosol (by binding GDIs, GDP dissociation inhibitors) and the membrane, and when on membranes, cycle between inactive (GDP-bound) and active (GTP-bound) states. This enables specificity of membrane localization of GTPases. This means that most interactions of proteins with GTPases are transient, and it

coefficient). (D) shows confocal micrograph. Data are mean ± SD (n = 3; graphs represent means of the triplicates from three independent experiments). Two-tailed paired t test, $^{**}p < 0.01$.

(E and F) HeLa cells were transfected with GFP-LC3 for 20 h and treated for 1 h with bafilomycin A1 followed by 4 h in HBSS (starvation), rapamycin (RAP) (1 μM), or SMER28 (20 μM). (E) Immunoprecipitates obtained by GFP-TRAP were processed for immunoblot for DNM2. (F) The amount of DNM2 co-immunoprecipitated with EGFP-LC3 was quantified and normalized for the amount of LC3 immunoprecipitated. Data are mean ± SD (n = 4; graphs represent means of four independent experiments). Two-tailed paired t test, $^{**}p < 0.01$.

(G) Recombinant DNM2 and LC3 proteins were incubated for 1 h at 25°C with gentle shaking. The mixture of the two proteins was immunoprecipitated using anti-DNM2 antibody and blotted for LC3 and DNM2. As control we immunoprecipitated DNM2 alone or LC3 alone. Note that recombinant LC3 levels in the input were below detection levels by western blotting.

(H) Representation of the different domains of DNM2. The LIR, identified using ILIR software (Jacomin et al., 2016), is shown.

(I) HeLa cells were transfected with DNM2 siRNA (oligo A and oligo B [see STAR Methods]) for 3 days. DNM2-silenced HeLa cells were transfected in the last 20 h with pEGFP-empty vector or with pEGFP-LC3 and HA-DNM2-WT or W525L. Immunoprecipitates obtained by GFP-TRAP were processed for immunoblot for DNM2. The histogram shows the amount of DNM2 co-immunoprecipitated with EGFP-LC3 normalized for the amount of LC3 immunoprecipitated. Data are mean ± SD (n = 4; graphs represent means of the triplicates from three independent experiments). Two-tailed paired t test, $^{****}p < 0.0001$.

(J) HeLa cells were silenced with siRNAs to DNM2 for 3 days and transfected for the last 20 h with DNM2-pEGFP-WT or W525L. The cells were fixed and labeled for endogenous LC3 and RAB11A. The histogram on the left shows the percentage of cells with RAB11A tubules. The histogram on the right shows the quantification of the association of LC3 with RAB11A or DNM2 with RAB11A (Manders' coefficient). Data are mean ± SD (n = 3 graphs represent means of the triplicates from three independent experiments). Two-tailed paired t test, $^{*}p < 0.05$, $^{**}p < 0.01$.

(K) HeLa cells transfected with DNM2 siRNA oligos (mix of oligos A and B) for 3 days, transfected for the last 20 h with HA-DNM2-WT or W525L, treated with DMSO (basal) or bafilomycin A1 (Baf) for 4 h, processed for immunoblot and labeled LC3, DNM2, and GAPDH as loading control. Histogram shows the relative amount of LC3-II in basal or under Baf treatment normalized for GAPDH. Data are mean ± SD (n = 3; graphs represent means of the triplicates from three independent experiments) two-tailed paired t test, $^{**} = p < 0.01$, ns, not significant. The numbers indicate the LC3-II/GAPDH value of the shown experiment.

(L) Ribbon representation of LC3B (PDB code: 5w9a) docked onto the PH domain of dynamin (PDB code: 5a3f). LC3B is colored green and PH domain of dynamin is colored cyan. Conserved LC3 residue R70 is colored in magenta and K51 is colored in orange. DNM2 W525 residue is colored in yellow. The figure was prepared using the program PyMOL (http://www.pymol.org).

(M) HeLa cells were transfected for 20 h with pEGFP-LC3-WT, K51A, or R70A. Immunoprecipitates obtained by GFP-TRAP were processed for immunoblot for DNM2. P62 was used as control. The histograms show the amount of DNM2 or P62 co-immunoprecipitated with EGFP-LC3, normalized for the amount of LC3 immunoprecipitated. Data are mean ± SD (n = 3 graphs represent means of the triplicates from three independent experiments). Two-tailed paired t test, $^{****}p < 0.0001$, $^{**}p < 0.01$, ns, not significant.

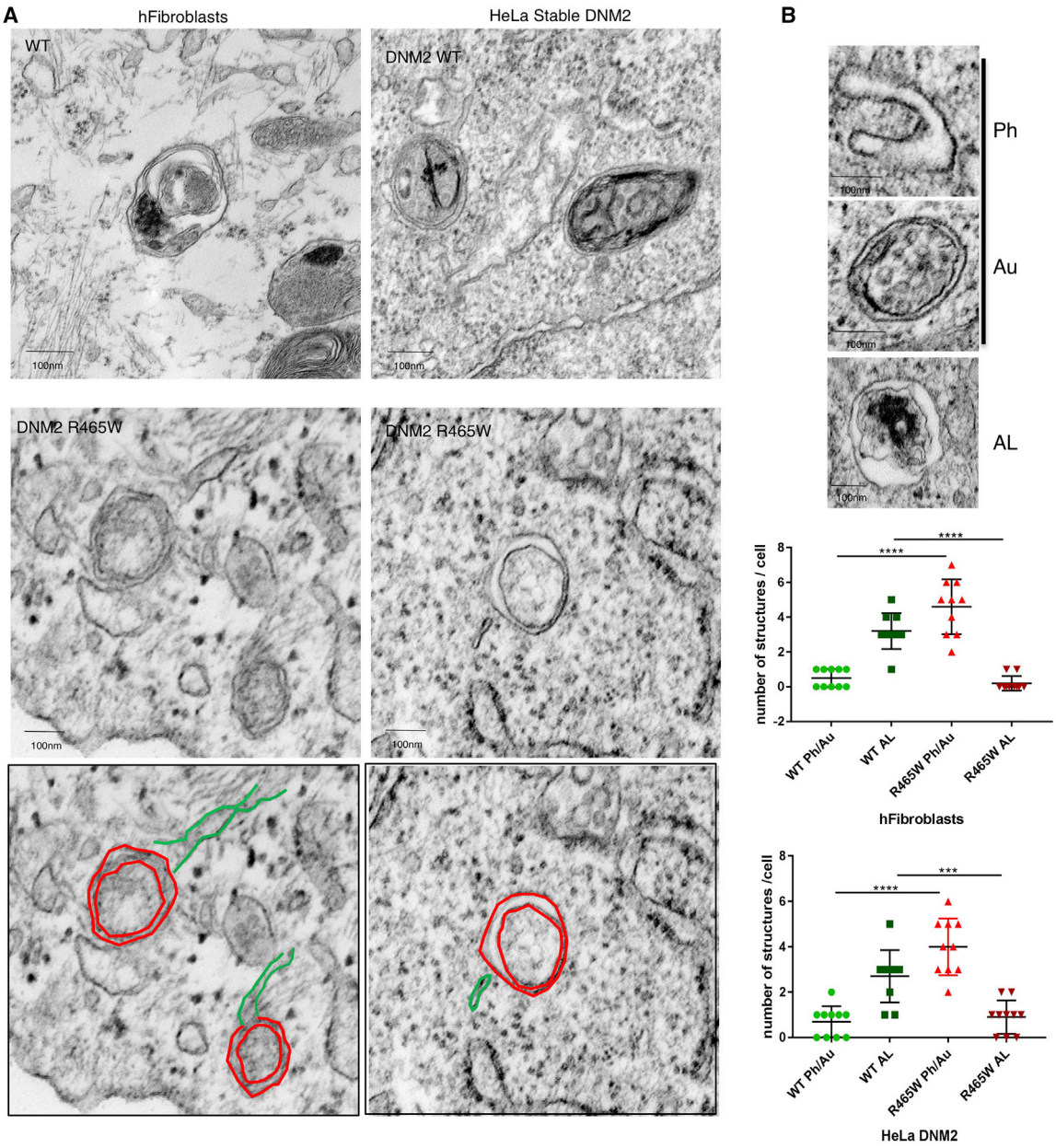

Figure 3. Cells Expressing DNM2 R465W Accumulate Immature Autophagosomes

(A and B) (A) WT or fibroblast from patients carrying DNM2 R465W mutation and HeLa stable cell lines expressing DNM2 WT or DNM2 R465W mutation were starved for 1 h and fixed for electron microscopy. The numbers of phagophores and autophagosomes (Ph/Au) or autolysosomes (AL) from 10 cell profiles were quantified with representative examples shown in (B). The histograms show the number of structures/cells. Data are mean ± SD (n = 10 cells each condition) two-tailed paired t test, ***p < 0.001, ****p < 0.0001.

Bottom panels of (A) show the electron microscopy (EM) images of the mutant (middle panels) outlining the autophagosomes (green) and the nearby tubules, which may be recycling endosomes.

is not surprising that they appear to be low (Antonny et al., 2016). Furthermore, DNM2 acts in a number of sites in the cell, and thus, it is not exclusively associated with a single partner.

Cells Expressing DNM2 R465W Accumulate Autophagosomes on Recycling Endosome

The DNM2 R465W centronuclear myopathy mutation causes an accumulation of immature autophagosomes (Durieux et al., 2012), which we confirmed both in patient fibroblasts (with endogenous protein) and in HeLa cells (with stably overexpressed WT or R465W DNM2), where we found that cells expressing R465W contained mainly phagophores and autophagosomes and very few autolysosomes, in contrast with WT cells that had mostly autolysosomal structures (Figures 3A and 3B). Mutant huntingtin exon 1 is a well-validated autophagy substrate and the proportions of cells with aggregates correlate directly

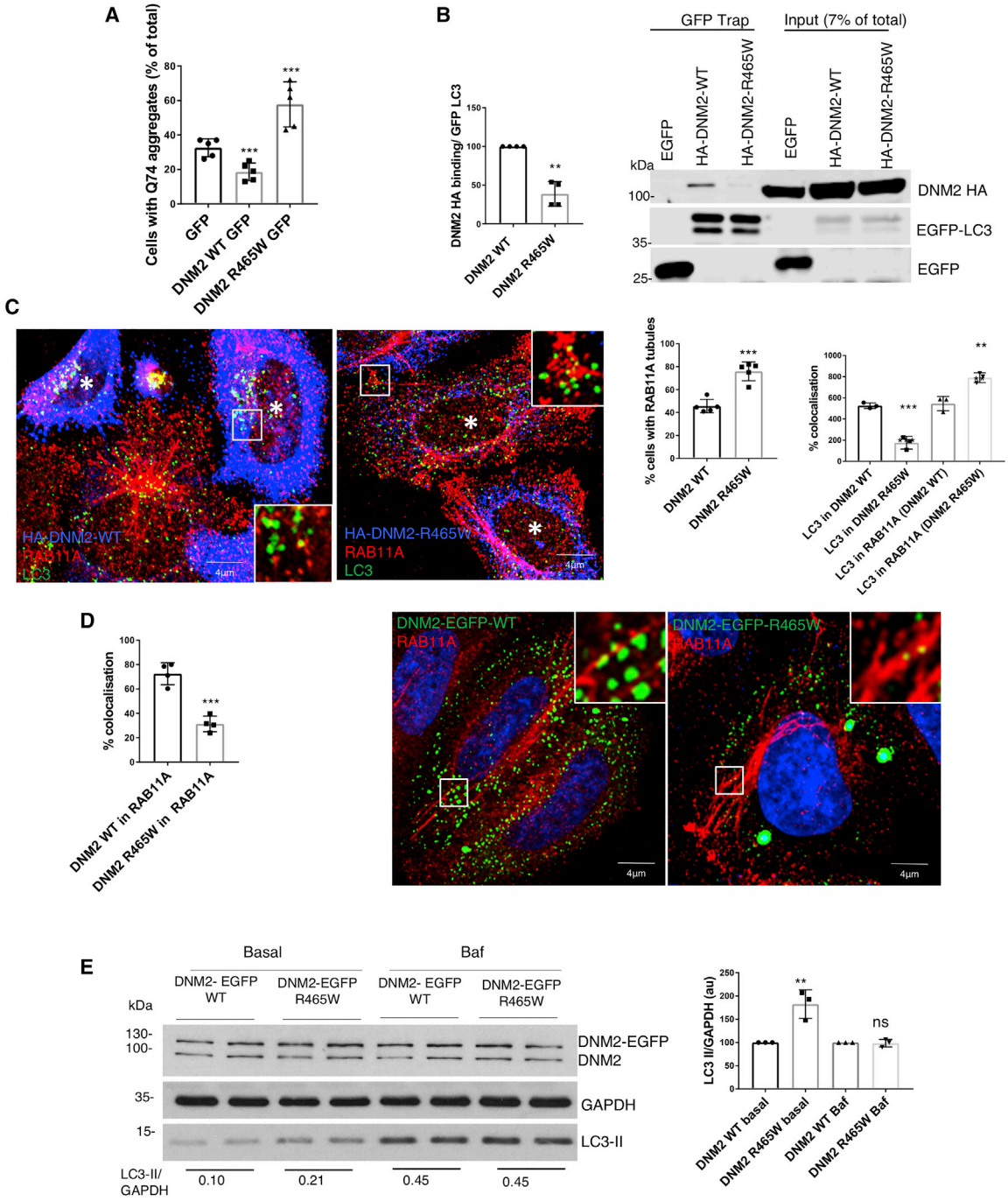

Figure 4. Cells Expressing DNM2 R465W Accumulate Autophagosomes on Recycling Endosomes

(A) HeLa cells were transfected with pEGFP-empty or pEGFP-DNM2-WT or R465W in combination with HA-tagged Htt-Q74 (mutant form of huntingtin associated with Huntington's disease) for 24 h and processed for immunofluorescence. Numbers of cells with Htt-Q74 aggregates are shown. Data are mean ± SD (n = 3, graphs represent means of the triplicates from three independent experiments). Two-tailed paired t test, ***p < 0.001.

(B) HeLa cells were transfected for 20 h with pEGFP-empty vector, or with pEGFP-LC3 and HA-DNM2-WT or HA-DNM2-R465W. Immunoprecipitates obtained by GFP-TRAP were processed for immunoblot for anti-HA. Note input is on right hand side of the gel. The histogram shows the amount of HA-DNM2 co-immunoprecipitated with pEGFP-LC3, normalized for the amount of LC3 immunoprecipitated. Data are mean ± SD (n = 3; graphs represent means of the triplicates from three independent experiments). Two-tailed paired t test, **p < 0.01.

(C) HeLa cells were transfected for 20 h with HA-DNM2-WT or R465W. The cells were fixed and labeled for anti-HA and endogenous LC3 and RAB11A. The histogram below on the right shows the quantification of the association of LC3 with DNM2 or LC3 with RAB11A (Manders' coefficient). The histogram on the left shows the percentage of cells with RAB11A tubules. Data are mean ± SD (n = 3; graphs represent means of the triplicates from three independent experiments). Two-tailed paired t test, **p < 0.01, ***p < 0.001.

(legend continued on next page)

with the levels of the protein, all other factors being equal (Narain et al., 1999). Overexpression of DNM2 R465W mutant increased the percentages of cells with aggregates of mutant huntingtin exon 1 (Q74 aggregates [Figure 4A]). The R465W mutation is not in the LIR domain yet binds much less LC3 in cells than the WT (Figure 4B). Overexpression of the DNM2 R465W mutant phenocopied cells with the DNM2-LIR mutant (Figure 2J) and caused an increase of the RAB11A tubules compared with overexpression of the WT (Figures 4C and S4A), decreased colocalization of LC3 with DNM2 R465W, increased colocalization of LC3 with RAB11A (Figure 4C), decreased DNM2-RAB11A colocalization (Figure 4D), and increased LC3-II in nutrient replete (Figure 4E) or starvation conditions but not with bafilomycin A1 (Figures S4B and S4C use DNM2 knockdown cells reconstituted with either WT or R465W).

Cells Expressing DNM2 Mutants Accumulate Immature Autophagosomes

DNM2 is an important component of the endocytic machinery. Importantly, endocytosis was normal in HeLa cells overexpressing DNM2 R465W (as it is also in the LIR mutant) and in cells where we used a 3-day knockdown protocol employed throughout this study, (which still leaves some residual DNM2) (Figure S5A). Our results are consistent with previous data using DNM2 R465W heterozygous mouse embryonic fibroblasts (MEFs) (Ali et al., 2019; Durieux et al., 2010). We observed similar normal localizations of ATG9A and ATG16L1 on RAB11A-positive structures (Puri et al., 2013) in cells expressing WT, R465W, or W525L forms of DNM2, suggesting that these mutants do not affect the trafficking of these ATG proteins (Figures 5A and S5B). We previously showed that ATG9A is trafficked from the plasma membrane to recycling endosomes (Puri et al., 2013). Using an antibody that we generated against the ATG9A II extracellular loop (validated in Figure S5C, we confirmed that the endocytosed ATG9A colocalized with LC3-positive structures (Figure S5D). We conjugated this anti-ATG9A antibody with micromagnetic beads (Ferrofluid) and allowed these conjugates to be endocytosed for 1 h and chased for 15 min (Puri et al., 2018a) into HeLa cells stably expressing WT, R465W, or W525L DNM2. The membranes containing the anti-ATG9A-Ferrofluid beads were separated magnetically (bound) and compared with the rest of the lysate (unbound). We confirmed that ATG9A was present in the bound fraction (as it is a multipass transmembrane protein) and that the amount of ATG16L1 in the bound fraction was very similar in DNM2 WT cells and the two mutants (Figures 5B and S5E), suggesting that the ATG9A trafficking leading to colocalization of ATG16L1 with ATG9A (Puri et al., 2013) was not affected by these DNM2 mutations. Moreover, both DNM2 mutants (W525L and R465W) were still able to bind SNX18 (sorting nexin 18) (Knævelsrud et al., 2013; Søreng et al., 2018) (Figure S5F), and since we did not observe abnormal ATG9A trafficking with R465W or W525L DNM2 (Figures 5A, 5B, S5B, and S5E), we concluded that the DNM2-LC3 biology is likely distinct from any effects of SNX18 in ATG9A trafficking from recycling endosomes (Figure S5F).

We thus tested if the DNM2 R465W and DNM2-LIR mutants (W525L) shared other autophagy phenotypes. We first transfected WT DNM2 or the two mutants in a HeLa stable cell line expressing the tandem tagged mRFP-GFP-LC3, which allows discrimination between non-acidified structures like autophagosomes/phagophores and acidified autolysosomes, since the former emit both RFP and GFP signals, whereas the acidic pH in lysosomes denatures GFP so that only RFP fluorescence is observed (Kimura et al., 2007). Both mutants caused a build-up of non-acidified structures at the expense of acidified structures, suggesting a block in autophagy upstream of autophagosome-lysosome fusion (Figures 5C and S5G). We also used the HaloTag-LC3 autophagosome completion assay that specifically detects phagophores, nascent autophagosomes, and mature autophagic structures by exploiting membrane-impermeable Alexa Fluor (AF) 488 HaloTag (MIL) and membrane-permeable tetramethylrhodamine HaloTag ligands (MPL) (Takahashi et al., 2018). This assay suggested that the mutants caused no change in the numbers of open phagophores, but led to an accumulation of autophagosomes and a reduction of autolysosomes, compatible with the mRFP-GFP-LC3 data above (Figures 5D and 5E). This defect is unlikely to be due to lysosomal defects, since cathepsin D maturation (which is impaired by raised lysosomal pH and some other defects) was similar in cells expressing WT and mutant forms of DNM2 (Figures 5F and S5H) or in DNM2 knockdown cells (Figure S5I). Interestingly, in cells transfected with DNM2 R465W, LC3 vesicles were not able to detach from the RAB11A-positive compartment, moved along the tubules and accumulated at the perinuclear region of the compartment (Figures S5J and S5K; Video S3). Thus, our data suggest that this mutant regulates the release of nascent autophagosomes from RAB11A-positive recycling endosomes.

ITSN1 Sequesters DNM2 R465W on Plasma Membrane

These data suggest that overexpression of DNM2 R465W compromises autophagy and mimics the autophagic phenotypes resulting from DNM2 loss-of-function or loss-of-LC3 binding—impaired release of LC3-containing membranes from the RAB11A compartment due to reduced scission. We wanted to resolve why the DNM2 R465W (CNM) mutant is not able to bind LC3 when the mutation is not in the DNM2 LIR domain. A clue emerged when immuno-electron microscopy showed DNM2 R465W in plaques on the plasma membrane (Figure 6A) and total internal reflection fluorescence (TIRF) microscopy revealed that DNM2 R465W localizes

(D) HeLa cells were transfected for 20 h with pEGFP-DNM2-WT or R465W. The cells were fixed and labeled for endogenous RAB11A. The histogram on the left shows the quantification of the association of DNM2 with RAB11A (Manders' coefficient). Data are mean ± SD (n = 3; graphs represent means of the triplicates from three independent experiments). Two-tailed paired t test, ***$p < 0.001$.

(E) HeLa cells transfected for 20 h with pEGFP-DNM2-WT or R465W were treated with DMSO (basal) or bafilomycin A1 (Baf) for 4 h, processed for immunoblot and labeled LC3, DNM2, and GAPDH as loading control. The histogram shows the relative amount of LC3-II in basal or under Baf treatment normalized for GAPDH. Data are mean ± SD (n = 3; graphs represent means of the triplicates from three independent experiments) two-tailed paired t test, **$p < 0.01$, ns, not significant. The numbers indicate the LC3-II/GAPDH value of the experiment shown.

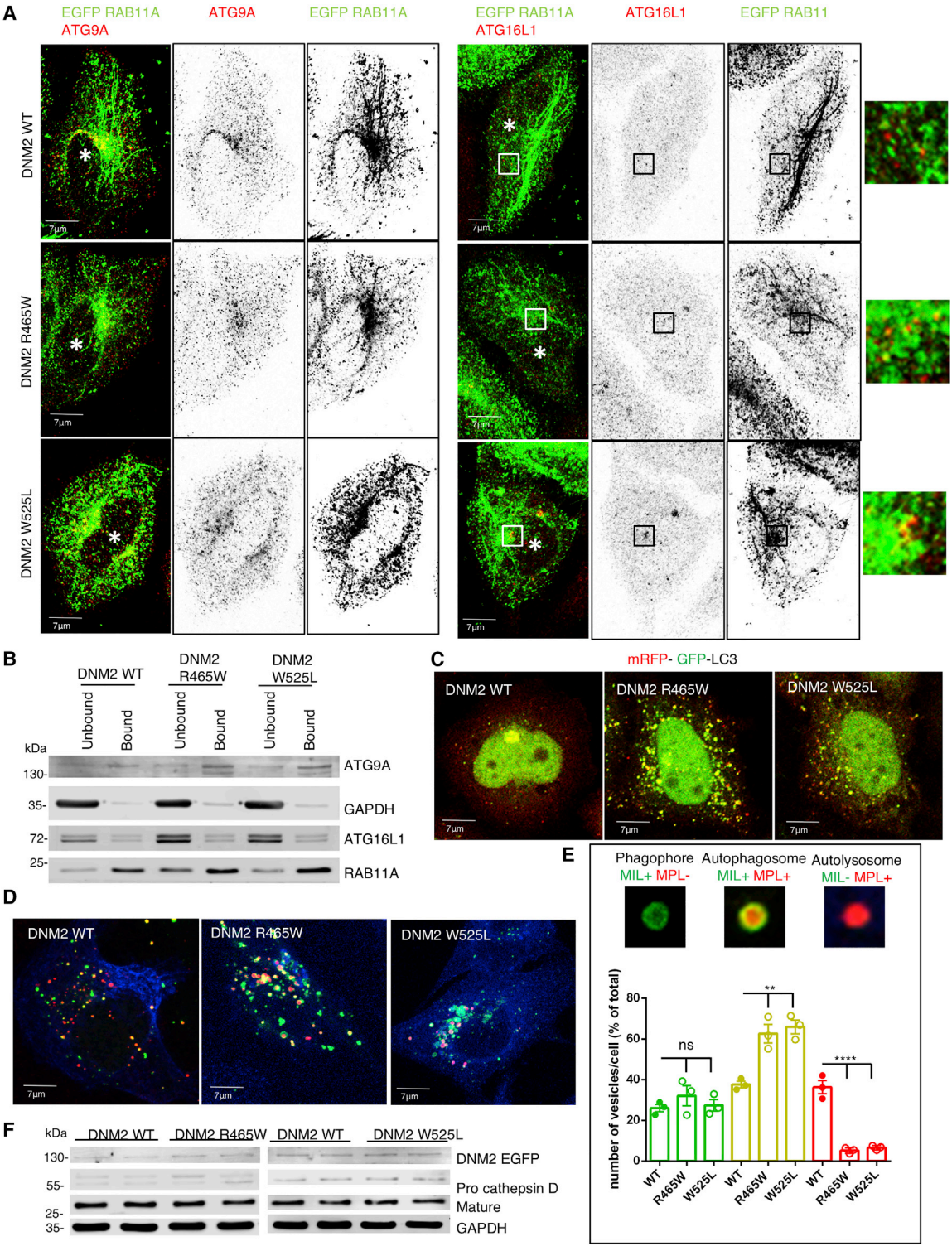

Figure 5. Cells Expressing DNM2 Mutants Accumulate Immature Autophagosomes

(A) HeLa cells were transfected for 20 h with HA-DNM2-WT or HA-DNM2-R465W or HA-DNM2-W525L and pEGFP-RAB11A and labeled for anti-HA and anti-ATG9A or anti-ATG16L1. The colocalizations between ATG9A or ATG16L1 with RAB11A were quantified and shown in Figure S5A.

(B) HeLa cells stably expressing DNM2-pEGFP-WT, DNM2-pEGFP-R465W, or DNM2-pEGFP-W525L were starved for 1 h in HBSS, loaded with ferrofluid-anti-ATG9A antibody for 1 h in HBSS and chased for 15 min in HBSS. The cells were then fragmented and the membranes containing ferrofluid-anti-ATG9A (bound) or not containing ferrofluid-anti-ATG9A (unbound) were separated, lysed, and processed for immunoblotting as indicated (see technical details in STAR Methods).

(legend continued on next page)

more with the clathrin adaptor AP2 on the plasma membrane than the WT protein (Figure 6B). On the plasma membrane, DNM2 interacts with intersectin 1 (ITSN1), a protein that acts as a scaffold for dynamin and other endocytic proteins ensuring its recruitment to sites of endocytosis (Sundborger and Hinshaw, 2014). Notably ITSN1 is not present on recycling endosomes (Figure S1A). We found that DNM2 R465W bound more ITSN1 than the WT (Figures 6C and 6D), which suggested that the DNM2 R465W mutant was not recruited to the site of autophagosome biogenesis (binds less LC3 [Figure 4B]) because it is sequestered away from the recycling endosome to the plasma membrane by ITSN1. This model was supported when we observed that while cells expressing the DNM2 R465W mutant have more RAB11A tubules-less fragmentation (Figure 4C), this phenotype was normalized when ITSN1 was depleted (Figures 6E and S6A). In cells overexpressing DNM2 R645W, ITSN1 knockdown reduced the amount of DNM2 R465W at the plasma membrane (by TIRF microscopy, Figures 6E, S6B, and S6C), recruited DNM2 R465W back to the recycling endosome (by superresolution SIM microscopy, Figure 6G), enabled DNM2 R465W-LC3 binding (Figure 6H) and increased autophagosome formation (LC3 level in basal and under bafilomycin A1 conditions [Figures 6I and S6D]). By contrast, when we silenced ITSN1 in cells reconstituted with the DNM2 LIR mutant (W525L), we observed no effect on LC3 levels, supporting the idea that the defect of LC3 binding for the DNM2 LIR mutant is independent of ITSN1 binding (Figure 6J). Thus, the DNM2 CNM R465W mutant, in contrast to the LIR mutant, is still able to bind LC3 efficiently and release autophagosomes from the recycling endosomes, but its mutation causes it to bind more to ITSN1, which diverts the CNM mutant to the plasma membrane to function in clathrin-mediated endocytosis, but away from recycling endosomes, thereby compromising release of the nascent autophagosomes.

R465W Fibroblasts Confirm the Phenotype Observed in HeLa Cells

We then verified the effects we observed above when we overexpressed the DNM2 CNM R465W mutation in MEFs from heterozygous mice and in fibroblasts from patients affected by CNM carrying the same mutation (Durieux et al., 2012, 2010). As we observed in HeLa cells in overexpression studies above, mouse and human fibroblasts with endogenous heterozygous expression of this CNM mutation had increased LC3-II in basal, but not under bafilomycin A1 conditions (Figures 7A and 7B), and increased of colocalization of LC3 with RAB11A (Figures S7A and 7B), suggesting defective release of LC3-positive structures from the RAB11A compartment. Depletion of ITSN1 in both human and mouse mutant fibroblasts restored normal autophagosome maturation in these mutant cells (increased LC3-II in the absence or presence of bafilomycin A [Figures 7C and 7D]).

ITSN1 Overexpression Phenocopies DNM2 CNM Mutation

If our hypothesis is correct, then overexpression of ITSN1 should negatively affect autophagy by sequestering DNM2 on the plasma membrane and phenocopy DNM2 loss of function as the CNM mutation. Consistent with this prediction, ITSN1 overexpression in normal cells blocked the release of LC3 from the recycling endosome compartment (increased colocalization of LC3 on RAB11A [Figures 7E, 7F, and S7C]) and increased recycling endosome tubulation-/decreased fragmentation (increased numbers of cells with RAB11A tubules Figure 7G). These phenotypes were associated with impaired autophagy, as measured by an increased percentage of cells with aggregates of mutant huntingtin exon 1 (Q74 aggregates [Figure 7H]), an increase of LC3-II in basal conditions and not under bafilomycin A1 (Figure 7I), and a decrease of DNM2-LC3 binding (Figure 7J).

DISCUSSION

Location, Location, Location

A major function of autophagy flux is to remove damaged mitochondria and unfolded proteins that are prone to aggregate. Indeed, muscles from autophagy-defective mice (ATG7−/−, ATG5−/−) reveal degenerative changes, including vacuolated and centrally nucleated myofibers similar to that described for CNM (Masiero et al., 2009; Yoshii et al., 2016). Our studies reveal an unusual mechanism for the DNM2 R465W CNM mutation. This mutant protein is functionally normal in that it has the capacity to bind LC3 and can mediate release of LC3-nascent autophagosomes from recycling endosomes. However, the mutation causes DNM2 sequestration by ITSN1 at the plasma membrane away from its LC3 binding sites at the recycling endosome—in this way it retains its functions in endocytosis but loses them in autophagy. The unusual mechanism for this mutation (which we have coined as the location, location, location mechanism) may be more common, as many proteins have multiple potentially competing partners. Our data also suggest that the mutant protein acts as a dominant-negative for this autophagic process, as DNM2 oligomerizes and we observed that overexpression phenocopied heterozygosity for the mutation and knockdown. This dominant-negative effect on autophagy is consistent with previous work showing that selective knockdown of the mutant allele in mice heterozygous for this mutation

(C) HeLa stable cell line expressing the tandem tagged mRFP-GFP-LC3 was transfected for 20 h with HA-DNM2-WT or HA-DNM2-R465W or HA-DNM2-W525L and labeled with anti-HA to visualize the transfected cells. The number of total vesicles or red-only vesicles were quantified and shown in Figure S5G.
(D and E) U-2 OS cells stably expressing HaloTag-LC3 (HT-LC3) were transfected for 20 h with HA-DNM2-WT or HA-DNM2-R465W or HA-DNM2-W525L and loaded with a combination of MIL and MPL and labeled for anti-HA. MIL+MPL (phagophores), MIL+MPL+ (nascent autophagosomes), and MIL−MPL+ (mature autophagosomes and autolysosomes) were quantified in HA-positive cells. (D) is representative confocal micrograph. (E) is histogram showing the number of structures/cells. Data are mean ± SD (n = 10 cells each condition) one-way ANOVA with post-hoc Tukey's test, **p < 0.01, ****p < 0.0001, ns, not significant.
(F) HeLa cells stably expressing DNM2-pEGFP-WT (WT), -R465W or -W525L were processed for western blot to analyze the amount of pro- or mature cathepsin D. The ratio of mature versus total cathepsin D was analyzed and the results are shown in Figure S5H.

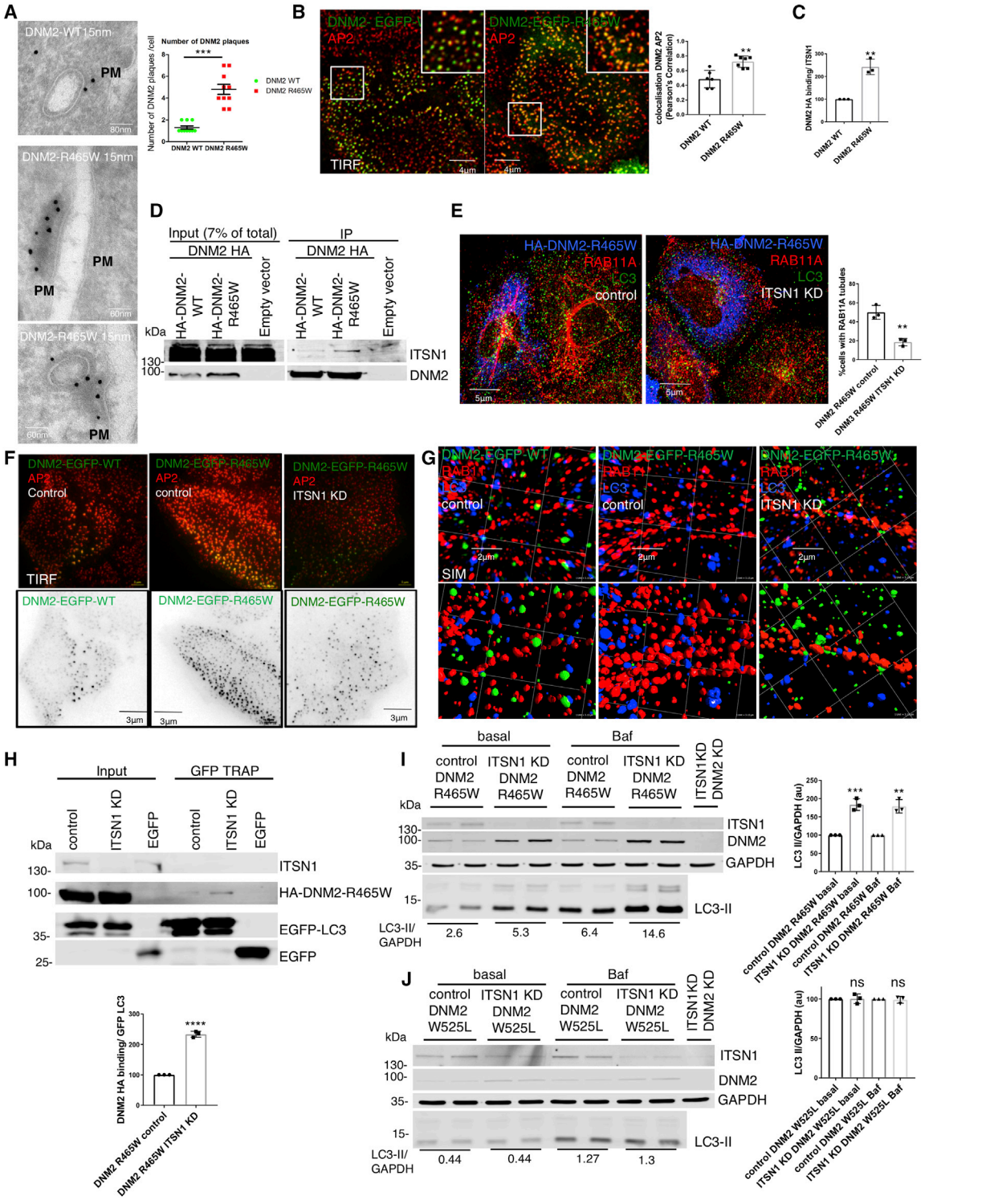

Figure 6. ITSN1 Sequesters DNM2 R465W on Plasma Membrane

(A) HeLa cells transfected with pEGFP-DNM2-WT or R465W for 24 h were fixed and treated for immunogold labeling on cryosections. EGFP-DNM2 was detected with anti-GFP antibody (15 nm gold). The number of DNM2 "plaques" on the plasma membrane present on 10 cell profiles was quantified. The histogram shows the number of DNM2 "plaques" on plasma membrane per cell. Data are mean ± SD (n = 10 cells each condition) two-tailed paired t test, ***$p < 0.001$.

(B) HeLa cells were transfected with pEGFP-empty or pEGFP-DNM2-WT or -R465W for 24 h, fixed and labeled for endogenous AP2 and processed for TIRF. The histogram on the right shows the quantification of the association of DNM2 with AP2 (Pearson's correlation). Data are mean ± SD (n = 7 cells each condition). Two-tailed paired t test, **$p < 0.01$.

(legend continued on next page)

ameliorates their muscle phenotypes (Buono et al., 2018; Trochet et al., 2018).

This mutation also reveals a new step in autophagy—the release of LC3-positive nascent autophagosomes from RAB11A-positive recycling endosomes. DNM2 is normally recruited to this compartment via a LIR-dependent interaction with LC3 after LC3 is conjugated to these membranes. DNM2 regulates scission of the recycling endosomes and this appears to be specific to the membrane sites where LC3 is conjugated. This tubule scission correlates with release of the LC3-positive autophagosomal structures. Previous literature has considered the key steps in autophagosome biogenesis to be induction, nucleation expansion, and closure (Yin et al., 2016). We believe that "scission" from the core platform on which LC3 conjugation occurs, the RAB11A-positive recycling endosomes, should be added as a step, as this process is critical, it is defective in a human disease and influences the way we consider how autophagosomes are formed. While we cannot exclude the possibility that this process may only have relevance to a subset of autophagosomes, we believe that it likely impacts most mammalian autophagosomes, since our previous data suggested that the RAB11A compartment and RAB11A-WIPI2 interactions are critical for autophagosome biogenesis (Puri et al., 2018a). Furthermore, our current data suggest major disruptions to the autophagosome itinerary occur when DNM2-mediated RAB11A-compartment scission is perturbed, as assessed by autophagic substrate levels and quantitation the maturation of different autophagic structures by electron microscopy, LC3 blots, mRFP-GFP-LC3, and HaloTag assays.

STAR★METHODS

Detailed methods are provided in the online version of this paper and include the following:

SUPPLEMENTAL INFORMATION

Supplemental Information can be found online at https://doi.org/10.1016/j.devcel.2020.03.018.

(C and D) HeLa cells were transfected for 20 h with empty vector or with HA-DNM2-WT or R465W. (D) The lysates were immunoprecipitated with anti-HA-conjugated magnetic beads and processed for immunoblots for anti-ITSN1. (C) The histogram shows the amount of ITSN1 co-immunoprecipitated with HA-DNM2-, normalized for the amount of HA-DNM2 immunoprecipitated. Data are mean ± SD (n = 3 graphs represent means of the triplicates from three independent experiments). Two-tailed paired t test, $^{**}p < 0.01$.

(E) HeLa cells transfected with control or ITSN1 siRNA oligos for 3 days were transfected for 20 h with HA-DNM2 R465W. The cells were fixed and labeled for anti-HA and endogenous LC3 and RAB11A. The histogram shows the percentage of cells with RAB11A tubules. Data are mean ± SD (n = 3, graphs represent means of the triplicates from three independent experiments). Two-tailed paired t test, $^{**}p < 0.01$. See also Figure S4A.

(F) HeLa cells transfected with control or ITSN1 siRNA oligos for 3 days were transfected in the last 20 h with HA-DNM2 WT or R465W. The cells were fixed and labeled for endogenous AP2 and processed for TIRF. The histogram in Figure S6C shows the quantification of the association of DNM2 with AP2 (Pearson's correlation).

(G) HeLa cells transfected with control or ITSN1 siRNA oligos for 3 days were transfected in the last 20 h with HA-DNM2 WT or R465W. The cells were labeled for endogenous RAB11A and LC3 and visualized on an Elyra (Zeiss) superresolution microscope. Top panels show the structured illumination image, while bottom panels show the isosurface rendering.

(H) HeLa cells transfected with control or ITSN1 siRNA oligos for 3 days then transfected in the last 20 h with HA-DNM2 R465W and pEGFP-LC3 or empty pEGFP vector. Immunoprecipitates obtained by GFP-TRAP were processed for immunoblot for anti-HA. The histogram below shows the amount of HA-DNM2 co-immunoprecipitated with EGFP-LC3, normalized for the amount of EGFP-LC3 immunoprecipitated. Data are mean ± SD (n = 3 graphs represent means of the triplicates from three independent experiments). Two-tailed paired t test, $^{****}p < 0.0001$.

(I) HeLa cells transfected with DNM2 and control or ITSN1 siRNA oligos for 3 days were then transfected in the last 20 h with HA-DNM2 R465W. The cells were treated with DMSO (basal) or bafilomycin A1 (Baf) for 4 h, processed for immunoblot and labeled LC3, HA-DNM2, and GAPDH as loading control. The histogram shows the relative amount of LC3-II in basal or under bafilomicyn A1 (Baf) treatment, normalized for GAPDH. Data are mean ± SD (n = 3, graphs represent means of the triplicates from three independent experiments) two-tailed paired t test, $^{**}p < 0.01$, $^{***}p < 0.001$. The numbers indicate the LC3-II/GAPDH value of the shown experiment.

(J) HeLa cells transfected with DNM2 and control or ITSN1 siRNA oligos for 3 days, were then transfected in the last 20 h with HA-DNM2 W525L. The cells were treated with DMSO (basal) or bafilomycin A1 (Baf) for 4 h, processed for immunoblot and labeled for LC3, HA-DNM2, and GAPDH as loading control. The histogram shows the relative amount of LC3-II in basal or under Baf treatment normalized for GAPDH. Data are mean ± SD (n = 3, graphs represent means of the triplicates from three independent experiments) two-tailed paired t test, ns, not significant. The numbers indicate the LC3-II/GAPDH value of the shown experiment.

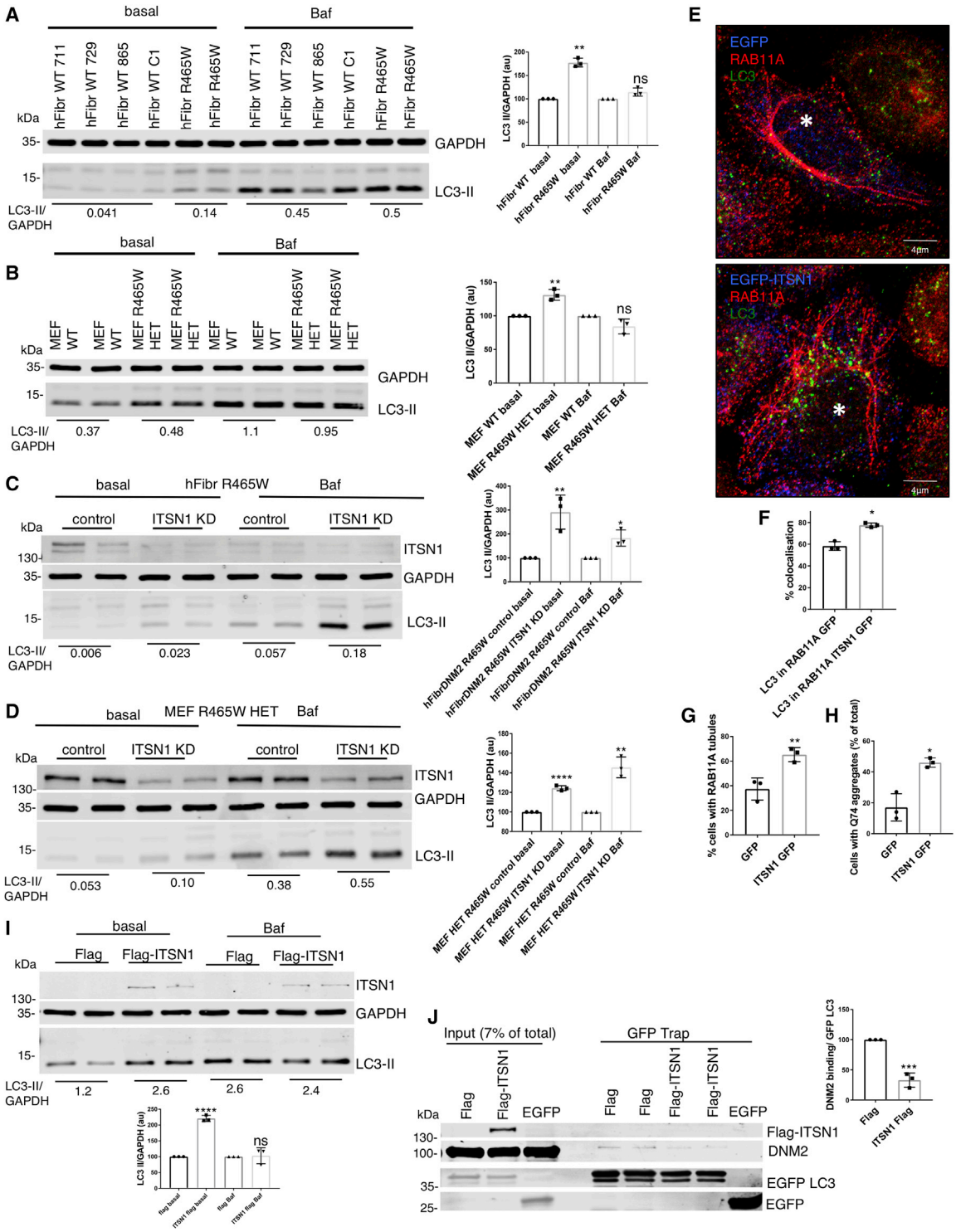

Figure 7. R465W Fibroblasts Confirm the Phenotype Observed in HeLa, and Overexpression of ITSN1 Mimics the Phenotype of DNM2 R465W Mutant

(A and B) (A) WT human fibroblasts and R465W mutant (from CNM patient) or (B) WT or R465W heterozygous (HET) MEFs were treated with DMSO (basal) or bafilomycin A1 (Baf) for 4 h, processed for immunoblot, and labeled LC3 and GAPDH as loading control. Histograms show the relative amount of LC3-II in basal or Baf treatment normalized for GAPDH. Data are mean ± SD (n = 3; graphs represent means of the triplicates from three independent experiments). Two-tailed paired t test, **p < 0.01, ns, not significant. The numbers indicate the LC3-II/GAPDH ratios of the representative blots.

(C and D) (C) WT human fibroblasts and R465W mutant (from CNM patient) or (D) WT or R465W HET MEFs transfected with control or ITSN1 siRNA oligos for 3 days. The fibroblasts were then treated with DMSO (basal) or bafilomycin A1 (Baf) for 4 h, processed for immunoblot, and labeled LC3 and GAPDH as loading

(legend continued on next page)

ACKNOWLEDGMENTS

We thank Matthew Gratian and Mark Bowen for technical assistance; Antonina Andreeva (MRC Laboratory of Molecular Biology, Cambridge, UK) for useful discussions; Tamotsu Yoshimori (Osaka University, Japan), Mark McNiven (Mayo Clinic and Mayo Graduate School Rochester, Minnesota, USA), and Anne Simonsen (Institute of Basic Medical Sciences-University of Oslo) for kindly providing reagents; and the Institute of Myology (Centre of Research in Myology, UMRS 974, F-75013, Paris, France) for providing the human fibroblasts from patients. We are grateful to the UK Dementia Research Institute (funded by the MRC, Alzheimer's Research UK, and the Alzheimer's Society) (D.C.R.), the Roger de Spoelberch Foundation (D.C.R.), Specialist Programme from Bloodwise (12048), the UK Medical Research Council (MC_U105161083 to Alan J. Warren) (C.H.), and the Commonwealth Scholarships Commission UK (G.R.).

AUTHOR CONTRIBUTIONS

Conceptualization, D.C.R. and C.P.; Methodology, C.P.; Investigation, C.P.; Writing – Original Draft, C.P. and D.C.R.; Writing – Review & Editing, C.P., M.M.M., M.V., C.H., Y.Z., G.R., E.S., F.M.M., K.M., M.B., and D.C.R; Funding Acquisition, D.C.R.; Resources, Y.Z., M.V., M.M.M., G.R., M.B., and K.M.; Supervision, D.C.R. and C.P.

DECLARATION OF INTERESTS

F.M.M. is employed by Eli Lilly, and D.C.R. is CSO of Aladdin Healthcare Technologies.

Received: August 21, 2019
Revised: January 24, 2020
Accepted: March 23, 2020
Published: April 20, 2020

WEB RESOURCES

PyMOL Software, http://www.pymol.org

REFERENCES

Ali, T., Bednarska, J., Vassilopoulos, S., Tran, M., Diakonov, I.A., Ziyadeh-Isleem, A., Guicheney, P., Gorelik, J., Korchev, Y.E., Reilly, M.M., et al. (2019). Correlative SICM-FCM reveals changes in morphology and kinetics of endocytic pits induced by disease-associated mutations in dynamin. FASEB J. *33*, 8504–8518.

Antonny, B., Burd, C., De Camilli, P., Chen, E., Daumke, O., Faelber, K., Ford, M., Frolov, V.A., Frost, A., Hinshaw, J.E., et al. (2016). Membrane fission by dynamin: what we know and what we need to know. EMBO J. *35*, 2270–2284.

Axe, E.L., Walker, S.A., Manifava, M., Chandra, P., Roderick, H.L., Habermann, A., Griffiths, G., and Ktistakis, N.T. (2008). Autophagosome formation from membrane compartments enriched in phosphatidylinositol 3-phosphate and dynamically connected to the endoplasmic reticulum. J. Cell Biol. *182*, 685–701.

Buono, S., Ross, J.A., Tasfaout, H., Levy, Y., Kretz, C., Tayefeh, L., Matson, J., Guo, S., Kessler, P., Monia, B.P., et al. (2018). Reducing dynamin 2 (DNM2) rescues DNM2-related dominant centronuclear myopathy. Proc. Natl. Acad. Sci. USA *115*, 11066–11071.

Catteruccia, M., Fattori, F., Codemo, V., Ruggiero, L., Maggi, L., Tasca, G., Fiorillo, C., Pane, M., Berardinelli, A., Verardo, M., et al. (2013). Centronuclear myopathy related to dynamin 2 mutations: clinical, morphological, muscle imaging and genetic features of an Italian cohort. Neuromuscul. Disord. *23*, 229–238.

Chino, H., Hatta, T., Natsume, T., and Mizushima, N. (2019). Intrinsically disordered protein TEX264 mediates ER-phagy. Mol. Cell *74*, 909–921.e6.

Dooley, H.C., Razi, M., Polson, H.E., Girardin, S.E., Wilson, M.I., and Tooze, S.A. (2014). WIPI2 links LC3 conjugation with PI3P, autophagosome formation, and pathogen clearance by recruiting Atg12-5-16L1. Mol. Cell *55*, 238–252.

Durieux, A.C., Vassilopoulos, S., Lainé, J., Fraysse, B., Briñas, L., Prudhon, B., Castells, J., Freyssenet, D., Bonne, G., Guicheney, P., and Bitoun, M. (2012). A centronuclear myopathy–dynamin 2 mutation impairs autophagy in mice. Traffic *13*, 869–879.

Durieux, A.C., Vignaud, A., Prudhon, B., Viou, M.T., Beuvin, M., Vassilopoulos, S., Fraysse, B., Ferry, A., Lainé, J., Romero, N.B., et al. (2010). A centronuclear myopathy-dynamin 2 mutation impairs skeletal muscle structure and function in mice. Hum. Mol. Genet. *19*, 4820–4836.

Eskelinen, E.L. (2019). Autophagy: supporting cellular and organismal homeostasis by self-eating. Int. J. Biochem. Cell Biol. *111*, 1–10.

Fass, E., Shvets, E., Degani, I., Hirschberg, K., and Elazar, Z. (2006). Microtubules support production of starvation-induced autophagosomes but not their targeting and fusion with lysosomes. J. Biol. Chem. *281*, 36303–36316.

Ferguson, S.M., and De Camilli, P. (2012). Dynamin, a membrane-remodelling GTPase. Nat. Rev. Mol. Cell Biol. *13*, 75–88.

Gao, W., Chen, Z., Wang, W., and Stang, M.T. (2013). E1-like activating enzyme Atg7 is preferentially sequestered into p62 aggregates via its interaction with LC3-I. PLoS One *8*, e73229.

Hamasaki, M., Furuta, N., Matsuda, A., Nezu, A., Yamamoto, A., Fujita, N., Oomori, H., Noda, T., Haraguchi, T., Hiraoka, Y., et al. (2013). Autophagosomes form at ER-mitochondria contact sites. Nature *495*, 389–393.

Hansen, M., Rubinsztein, D.C., and Walker, D.W. (2018). Autophagy as a promoter of longevity: insights from model organisms. Nat. Rev. Mol. Cell Biol. *19*, 579–593.

control. The histogram shows the relative amount of LC3-II in basal or under Baf treatment normalized for GAPDH. Data are mean ± SD (n = 3, graphs represent means of the triplicates from three independent experiments) two-tailed paired t test, *p < 0.05, **p < 0.01, ****p < 0.0001. The numbers indicate the LC3-II/GAPDH values of the representative blots.

(E–G) HeLa cells were transfected for 20 h with pEGFP-ITSN1 or pEGFP-empty vector. The cells were fixed for endogenous LC3 and RAB11A. The histogram in (F) shows the quantification of the association of LC3 with RAB11A (Manders' coefficient). The histogram in (G) shows the percentage of cells with RAB11A tubules. Data are mean ± SD (n = 3, graphs represent means of the triplicates from three independent experiments). Two-tailed paired t test, *p < 0.05, **p < 0.01.

(H) HeLa cells were transfected with pEGFP-ITSN1 or pEGFP-empty vector in combination with HA-tagged Htt-Q74 (mutant form of huntingtin associated with Huntington's disease) for 24 h and processed for immunofluorescence. The percentages of cells with Htt-Q74 aggregates are shown. Data are mean ± SD (n = 3; graphs represent means of the triplicates from three independent experiments). Two-tailed paired t test, *p < 0.05.

(I) HeLa cells transfected for 20 h with flag-ITSN1 or flag-empty vector were treated with DMSO (basal) or bafilomycin A1 (Baf) for 4 h, processed for immunoblot, and labeled anti-Flag, LC3, and GAPDH as loading control. The histogram shows the relative amount of LC3-II in basal or under Baf treatment normalized for GAPDH. Data are mean ± SD (n = 3; graphs represent means of the triplicates from three independent experiments). Two-tailed paired t test, ****p < 0.0001, ns, not significant. The numbers indicate the LC3-II/GAPDH values of the representative blot.

(J) HeLa cells transfected for 20 h with flag-ITSN1 or empty-flag vector and pEGFP-LC3 or pEGFP-empty vector. Immunoprecipitates obtained by GFP-TRAP were processed for immunoblot for DNM2. The histogram shows the amount of DNM2 co-immunoprecipitated with pEGFP-LC3 normalized for the amount of EGFP-LC3 immunoprecipitated. Data are mean ± SD (n = 3 graphs represent means of the triplicates from three independent experiments). Two-tailed paired t test, ***p < 0.001.

Hayashi-Nishino, M., Fujita, N., Noda, T., Yamaguchi, A., Yoshimori, T., and Yamamoto, A. (2009). A subdomain of the endoplasmic reticulum forms a cradle for autophagosome formation. Nat. Cell Biol. *11*, 1433–1437.

Hohendahl, A., Roux, A., and Galli, V. (2016). Structural insights into the centronuclear myopathy-associated functions of BIN1 and dynamin 2. J. Struct. Biol. *196*, 37–47.

Izumi, H., Li, Y., Shibaki, M., Mori, D., Yasunami, M., Sato, S., Matsunaga, H., Mae, T., Kodama, K., Kamijo, T., et al. (2019). Recycling endosomal CD133 functions as an inhibitor of autophagy at the pericentrosomal region. Sci. Rep. *9*, 2236.

Jacomin, A.C., Samavedam, S., Promponas, V., and Nezis, I.P. (2016). iLIR database: A web resource for LIR motif-containing proteins in eukaryotes. Autophagy *12*, 1945–1953.

Kabeya, Y., Mizushima, N., Ueno, T., Yamamoto, A., Kirisako, T., Noda, T., Kominami, E., Ohsumi, Y., and Yoshimori, T. (2000). LC3, a mammalian homologue of yeast Apg8p, is localized in autophagosome membranes after processing. EMBO J. *19*, 5720–5728.

Kimura, S., Noda, T., and Yoshimori, T. (2007). Dissection of the autophagosome maturation process by a novel reporter protein, tandem fluorescent-tagged LC3. Autophagy *3*, 452–460.

Knævelsrud, H., Carlsson, S.R., and Simonsen, A. (2013a). SNX18 tubulates recycling endosomes for autophagosome biogenesis. Autophagy *9*, 1639–1641.

Knævelsrud, H., Søreng, K., Raiborg, C., Håberg, K., Rasmuson, F., Brech, A., Liestøl, K., Rusten, T.E., Stenmark, H., Neufeld, T.P., et al. (2013b). Membrane remodeling by the PX-BAR protein SNX18 promotes autophagosome formation. J. Cell Biol. *202*, 331–349.

Korolchuk, V.I., Mansilla, A., Menzies, F.M., and Rubinsztein, D.C. (2009). Autophagy inhibition compromises degradation of ubiquitin-proteasome pathway substrates. Mol. Cell *33*, 517–527.

Longatti, A., Lamb, C.A., Razi, M., Yoshimura, S., Barr, F.A., and Tooze, S.A. (2012). TBC1D14 regulates autophagosome formation via Rab11- and ULK1-positive recycling endosomes. J. Cell Biol. *197*, 659–675.

Masiero, E., Agatea, L., Mammucari, C., Blaauw, B., Loro, E., Komatsu, M., Metzger, D., Reggiani, C., Schiaffino, S., and Sandri, M. (2009). Autophagy is required to maintain muscle mass. Cell Metab. *10*, 507–515.

Menzies, F.M., Fleming, A., Caricasole, A., Bento, C.F., Andrews, S.P., Ashkenazi, A., Füllgrabe, J., Jackson, A., Jimenez Sanchez, M., Karabiyik, C., et al. (2017). Autophagy and neurodegeneration: pathogenic mechanisms and therapeutic opportunities. Neuron *93*, 1015–1034.

Narain, Y., Wyttenbach, A., Rankin, J., Furlong, R.A., and Rubinsztein, D.C. (1999). A molecular investigation of true dominance in Huntington's disease. J. Med. Genet. *36*, 739–746.

Peden, A.A., Schonteich, E., Chun, J., Junutula, J.R., Scheller, R.H., and Prekeris, R. (2004). The RCP-Rab11 complex regulates endocytic protein sorting. Mol. Biol. Cell *15*, 3530–3541.

Puri, C., Renna, M., Bento, C.F., Moreau, K., and Rubinsztein, D.C. (2013). Diverse autophagosome membrane sources coalesce in recycling endosomes. Cell *154*, 1285–1299.

Puri, C., Vicinanza, M., Ashkenazi, A., Gratian, M.J., Zhang, Q., Bento, C.F., Renna, M., Menzies, F.M., and Rubinsztein, D.C. (2018a). The RAB11A-positive compartment is a primary platform for autophagosome assembly mediated by WIPI2 recognition of PI3P-RAB11A. Dev. Cell *45*, 114–131.e8.

Puri, C., Vicinanza, M., and Rubinsztein, D.C. (2018b). Phagophores evolve from recycling endosomes. Autophagy *14*, 1475–1477.

Ravikumar, B., Moreau, K., Jahreiss, L., Puri, C., and Rubinsztein, D.C. (2010). Plasma membrane contributes to the formation of pre-autophagosomal structures. Nat. Cell Biol. *12*, 747–757.

Ross, J.A., Digman, M.A., Wang, L., Gratton, E., Albanesi, J.P., and Jameson, D.M. (2011). Oligomerization state of dynamin 2 in cell membranes using TIRF and number and brightness analysis. Biophys. J. *100*, L15–L17.

Shibutani, S.T., and Yoshimori, T. (2014). A current perspective of autophagosome biogenesis. Cell Res. *24*, 58–68.

Søreng, K., Munson, M.J., Lamb, C.A., Bjørndal, G.T., Pankiv, S., Carlsson, S.R., Tooze, S.A., and Simonsen, A. (2018). SNX18 regulates ATG9A trafficking from recycling endosomes by recruiting Dynamin-2. EMBO Rep. *19*, e44837.

Sundborger, A.C., and Hinshaw, J.E. (2014). Regulating dynamin dynamics during endocytosis. F1000Prime Rep. *6*, 85.

Takahashi, Y., He, H., Tang, Z., Hattori, T., Liu, Y., Young, M.M., Serfass, J.M., Chen, L., Gebru, M., Chen, C., et al. (2018). An autophagy assay reveals the ESCRT-III component CHMP2A as a regulator of phagophore closure. Nat. Commun. *9*, 2855.

Tang, D., Kang, R., Berghe, T.V., Vandenabeele, P., and Kroemer, G. (2019). The molecular machinery of regulated cell death. Cell Res *29*, 347–364.

Trochet, D., Prudhon, B., Beuvin, M., Peccate, C., Lorain, S., Julien, L., Benkhelifa-Ziyyat, S., Rabai, A., Mamchaoui, K., Ferry, A., et al. (2018). Allele-specific silencing therapy for dynamin 2-related dominant centronuclear myopathy. EMBO Mol. Med. *10*, 239–253.

Tung, Y.T., Hsu, W.M., Lee, H., Huang, W.P., and Liao, Y.F. (2010). The evolutionarily conserved interaction between LC3 and p62 selectively mediates autophagy-dependent degradation of mutant huntingtin. Cell. Mol. Neurobiol. *30*, 795–806.

van Dam, E.M., and Stoorvogel, W. (2002). Dynamin-dependent transferrin receptor recycling by endosome-derived clathrin-coated vesicles. Mol. Biol. Cell *13*, 169–182.

Vicinanza, M., Korolchuk, V.I., Ashkenazi, A., Puri, C., Menzies, F.M., Clarke, J.H., and Rubinsztein, D.C. (2015). PI(5)P regulates autophagosome biogenesis. Mol. Cell *57*, 219–234.

Yin, Z., Pascual, C., and Klionsky, D.J. (2016). Autophagy: machinery and regulation. Microb. Cell *3*, 588–596.

Ylä-Anttila, P., Vihinen, H., Jokitalo, E., and Eskelinen, E.L. (2009). 3D tomography reveals connections between the phagophore and endoplasmic reticulum. Autophagy *5*, 1180–1185.

Yoshii, S.R., Kuma, A., Akashi, T., Hara, T., Yamamoto, A., Kurikawa, Y., Itakura, E., Tsukamoto, S., Shitara, H., Eishi, Y., and Mizushima, N. (2016). Systemic analysis of Atg5-null mice rescued from neonatal lethality by transgenic ATG5 expression in neurons. Dev. Cell *39*, 116–130.

Zhao, M., Maani, N., and Dowling, J.J. (2018). Dynamin 2 (DNM2) as cause of, and modifier for, human neuromuscular disease. Neurotherapeutics *15*, 966–975.

STAR★METHODS

KEY RESOURCES TABLE

REAGENT or RESOURCE	SOURCE	IDENTIFIER
Antibodies		
mouse anti AP2	Thermofisher	Cat#(MA1-064) AB_2258307
rabbit anti-ATG3	ABCAM	Cat#(ab108251) AB_10865145
rabbit anti-ATG9A	ABCAM	Cat#(ab108338) AB_10863880
rabbit anti-ATG9A	Eurogentec	rabbit 1963 (This paper)
rabbit anti-ATG16L1	Cell Signaling	Cat#(D6D5) AB_10950320
mouse anti-Cathepsin D	ABCAM	Cat#(ab6313) AB_305416
rabbit anti DNM2	ABCAM	Cat#(ab65556) AB_1603781
mouse anti-Flag	SIGMA	Cat#(F1804) AB_262044
rabbit anti-GABARAP	GENERON	Cat#(AP1821A) AB_2278762
rabbit anti-GABARAP-L1	Proteintech	Cat#(110101) AB_2294415
GABARAP-L2	MBL	Cat#(PM038) AB_843130
mouse anti-GAPDH	ABCAM	Cat#(ab8245) AB_2107448
rabbit anti-GFP	Invitrogen	Cat#(A6455) AB_221570
mouse anti-HA	Biolegend	Cat#(16B12) AB_10063630
rabbit anti-ITSN1	Millipore	Cat#(ABN1378)
mouse anti-LC3B	Nanotools	Cat#(0231-100/LC3-5F10) AB_2722733
rabbit anti-LC3B	ABCAM	Cat#(ab192890)
rabbit anti-P62	MBL	Cat#(PM045) AB_1279301
mouse anti-Myc tag	ABCAM	ab18185 AB_444307
rabbit anti-RAB11A	ABCAM	Cat# (ab128913) AB_11140633
Chemicals, Peptides, and Recombinant Proteins		
Ferrofluid EMG508	Megatech ltd.	Cat# (TSD-06-24-11-1)
Bafilomycin A1	Enzo	Cat# (BML-CM110)
SMER28	Tocris	Cat# (4297)
Rapamycin	LC Laboratories	Cat# (R-5000)
HaloTag TMR ligand	Promega	Cat# (G825A)
HaloTag Alexa 488 ligand	Promega	Cat# (G100A)
Seahorse XF Plasma membrane permeabilizer	Agilent Technologies	Cat# (102504-100)
DNM2 recombinant protein	Origene,	Cat# (TP323585)
LC3 recombinant protein	This paper	N/A

(*Continued on next page*)

Continued

REAGENT or RESOURCE	SOURCE	IDENTIFIER
Critical Commercial Assays		
GFP-TRAP	Chromotek	Cat# (Gtma-20)
Myc-TRAP	Chromotek	Cat# (ytma-20)
Anti-HA Magnetic Beads	Pierce	Cat# (88836)
Experimental Models: Cell Lines		
U2OS Halotag-LC3	This paper	N/A
HeLa DNM2-PEGFP WT	This paper	N/A
HeLa DNM2-PEGFP R465W	This paper	N/A
HeLa DNM2-PEGFP W525L	This paper	N/A
RFP-GFP tandem fluorescent-tagged LC3	Ravikumar et al., 2010	N/A
Mouse embryonic fibroblasts DNM2R465W	Durieux et al., 2010	N/A
Mouse embryonic fibroblasts WT	Durieux et al., 2010	N/A
Patient-derived fibroblasts DNM2 R465W	Trochet et al., 2018	N/A
Control human fibroblasts C1	Trochet et al., 2018	N/A
Control human fibroblasts 711	Coriell Institute	GM04711
Control human fibroblasts 729	Coriell Institute	GM04729
Control human fibroblasts 865	Coriell Institute	GM04865
Oligonucleotides (primers)		
Primer for DNM2 R465W: TCA CCA CCT ACA TCT GGG AGC GAG AAG GG	This paper	N/A
Primer for DNM2 W525L: TGA TCC GCA GGG GCT TGT TGA CCA TCA ACA AC	This paper	N/A
Primer for LC3 K51A: CCG TCC TGG ACA AGA CCG CGT TCC TTG TAC CTG ATC	This paper	N/A
Primer for LC3 R70A: CAT CAA GAT AAT TAG AAG GGC CCT GCA GCT CAA TGC TAA C	This paper	N/A
For siRNA sequences, see Table S1		
Recombinant DNA		
pEGFP-RAB11A	Puri et al., 2013	N/A
mCherry-RAB11A	Puri et al., 2018a	N/A
pEGFP-LC3	Tamotsu Yoshimori (Osaka University, Japan)	N/A
pECFP-LC3	Tamotsu Yoshimori (Osaka University, Japan)	N/A
RFP-LC3	Tamotsu Yoshimori (Osaka University, Japan)	N/A
LC3-PGEX-6P-1	Mineyuki Mizuguchi (Toyama University, Japan)	N/A
DNM2-WT-PEGFP	Mark McNiven (Mayo Clinic Minnesota, USA)	N/A
HA -DNM2-WT	Addgene	Cat# (34684)
Flag-ITSN1-short	Addgene	Cat# (47392)
pEGFP-ITSN1 short	Addgene	Cat# (47394)
Flag-empty vector	SIGMA	Cat# (E4901)
Myc-SNX18-WT	Anne Simonsen (University of Oslo, Norway)	N/A
Myc-SNX18- W38F	Anne Simonsen (University of Oslo, Norway)	N/A
httQ74-HA	Korolchuk et al., 2009	N/A
Software and Algorithms		
Prism 7	GraphPad	N/A
ZEN Black	Carl Zeiss Microscopy	N/A
Volocity	PerkinElmer	N/A
Image Studio Lite	LI-COR, Inc	N/A
ImageJ	National Institute of Health, USA	N/A

RESOURCE AVAILABILITY

Lead Contact

Further information and requests for resources and reagents should be directed to and will be fulfilled by the Lead Contact, David C Rubinsztein (dcr1000@cam.ac.uk).

Materials Availability

Plasmids generated in this study will be deposited to Addgene. In the meanwhile, we will make plasmids and cell lines that we have generated available through requests to the lead contact/corresponding author.

Data and Code Availability

This study did not generate datasets or code.

EXPERIMENTAL MODEL AND SUBJECT DETAILS

Cell Culture

HeLa cells were cultured in Dulbecco's modified Eagle's medium (DMEM) (SIGMA D6548) supplemented with 2 mM L-glutamine, 100 U/ml Penicillin/Streptomycin and 10% Fetal Bovine Serum in 5% CO_2 at 37°C. Human fibroblasts and Mouse Embryonic Fibroblasts (MEF) were cultured in Dulbecco's modified Eagle's medium-GlutMAX (Gibco 31966) supplemented with 2 mM L-glutamine, 100 U/ml Penicillin/Streptomycin and 20% Fetal Bovine Serum, Sodium Pyruvate (SIGMAS8636) and Non-essential amino acids (SIGMA M7145).

Stable Cell Line

U2OS Halotag-LC3

Halotag-LC3 (MAP1LC3B) constructs were purchased from the Kazusa collection (Promega). Plasmid DNA was digested with Sco1 and the linear DNA fragment encoding the tagged LC3 along with the CMV promoter was gel-extracted. U2OS cells were grown in a 6 well plate until 80% confluent and cells were transfected with 1ug linear plasmid DNA, 100 ng linear hygromycin marker (Clontech) 10 ug Nupherin and 4 ul Mirus transfection reagent per well, and in control wells no DNA was added. When confluent, each well was split into a 10 cm culture dish and media was supplemented with 100 ug/ml hygromycin. Cells were maintained until all cells in control dishes were dead. In order to generate single cell clones, cells in culture were labelled with diAcFam Halotag ligand (Promega) following manufacturer's instructions. Halotag expressing (labelled) cells were selected by FACS and sorted into 96 well plates with one cell per well. Single cells were then expanded to generate clonal cell lines. Expression of Halotag-LC3 was confirmed by two methods; cells were lysed and assessed by western blotting using LC3 antibody to confirm the presence of a band at the expect molecular weight, and cells were labelled with TMR Halotag ligand (Promega), lysed and run on an agarose gel. The gel was then scanned on a Typhoon Trio Imager Scanner to detect the fluorescently labelled Halotag protein and confirm the molecular weight.

HeLa DNM2-PEGFP WT and Mutants

HeLa cells were transfected with GFP- DNM2-PEGFP WT and mutant constructs (Puri et al., 2013). After 24 h, the cells were placed in selection medium (DMEM supplemented with 0.5 μg/ml G418) for 10 days. The antibiotic-resistant cells were then FACS sorted to isolate the GFP-expressing population. The cells were maintained in culture with DMEM supplemented with 0.5 μg/ml G418. HeLa cells stably expressing GFP- DNM2-PEGFP WT and mutants were maintained in culture with DMEM supplemented with 0.6 μg/ml G418, as previously described (Ravikumar et al., 2010).

METHOD DETAILS

Antibodies and Reagents

The antibodies used were: mouse anti AP2 (AP6 clone MA1-064 Thermofisher 1: 200 for IF), rabbit anti-ATG3 (ab108251-ABCAM; 1:200 for IF), rabbit anti-ATG9A (ab108338-ABCAM 1:200 for IF), rabbit anti-ATG16L1 (D6D5-Cell Signaling f; 1:200 for immunofluorescence), mouse anti-Cathepsin D (ab6313- ABCAM for WB 1:100), rabbit anti DNM2 (ab65556 ABCAM 1:1000 immunoblot), mouse anti-Flag (clone M2 SIGMA F1804 1:100 for immunoblot), rabbit anti-GABARAP (AP1821A-GENERON; for IP 1:140 and WB1:1000), rabbit anti-GABARAP-L1 (110101-Proteintech; for IP 1:140 and WB1:1000), rabbit anti-GABARAP-L2 (PM038-MBL; for IP 1:140 and WB1:1000), mouse anti-GAPDH (ab8245-ABCAM; 1:5000 for immunoblot), rabbit anti-GFP (A6455-Invitrogen; 1:100 for EM), mouse anti-HA (16B12- Biolegend; 1:400 for IF and immunoblot), rabbit anti-ITSN1 (ABN1378 Millipore 1:100 immunoblot), mouse anti-LC3B (0231-100/LC3-5F10-Nanotools; 1:200 for IF), rabbit anti-LC3B (ab192890-ABCAM; 1:200 for IF and immunoblot), rabbit anti-P62 (MBL PM045; 1:1000 for immunoblot), mouse anti-Myc tag(ab18185-ABCAM), rabbit anti-RAB11A (ab128913-ABCAM; 1:1000 for immunoblot and 1:200 for IF), Ferrofluid EMG508 is from Megatech ltd. (TSD-06-24-11-1). GFP-TRAP and Myc-TRAP are from Chromotek, Anti-HA Magnetic Beads (Pierce 88836). Protein-A gold is from CMC (Utrecht- NL), human transferrin Alexa-647 (T23366) and Alexa-488 (T13342) (Thermofisher), HaloTag TMR ligand (Promega G825A), HaloTag Alexa 488 ligand (Promega G100A) and Seahorse XF Plasma membrane permeabilizer (Agilent Technologies 102504-100).

All the secondary antibodies for immunofluorescence and LICOR are from Thermofisher.

Drug treatments used include: 400 nM Bafilomycin-A1 (Enzo, BML-CM110).

The rabbit antibody anti-ATG9A (1963) (aa 42-57 in the loop 2: Ac- SRLNRGYKPASKYMNC -NH2) was made by Eurogentec (for FerroFluid 1:20 (100 ul in 2 ml Serum free medium with 5 ul FerroFluid) and WB 1:1000).

Plasmids

pEGFP-RAB11A, mCherry-RAB11A, have been described elsewhere (Puri et al., 2013); pEGFP-LC3, pECFP-LC3, mRFP-LC3 were a kind gift from Tamotsu Yoshimori (Osaka University, Japan), LC3-PGEX-6P-1 was a gift from Mineyuki Mizuguchi (Faculty of Pharmaceutical Sciences, Toyama Medical and Pharmaceutical University, Laboratory of Structual Biology), DNM2-WT-PEGFP- was a gift from Mark McNiven (Mayo Clinic and Mayo Graduate School Rochester, Minnesota, USA), HA -DNM2-WT (Addgene-34684), Flag-ITSN1-short (Addgene 47392), pEGFP-ITSN1 short (Addgene 47394), Flag-empty vector (SIGMA-E4901), Myc-SNX18-WT and W38F was a kind gift from Anne Simonsen (Institute of Basic Medical Sciences- University of Oslo).

Mutagenesis

All LC3 and DNM2 mutant were generated by using a QuikChange Lightning Multisite-Directed Mutagenesis kit (Agilent Technologies 210515-5) according to the manufacturer's instructions.

Cell Transfection

The cells were seeded at 1-2 x105 per 6-well and transfections were performed using LipofectAMINE 2000 for siRNA, according to the manufacturer's instructions, using 100 nM siRNA. All the DNA constructs were transfected using Mirus Bio TransIT ®-2020, at 1 μg per well of a 6-well plate.

Western Blot Analysis

HeLa cells were lysed in Laemmli buffer. Protein samples were boiled for 5–7 minutes at 100°C, separated by SDS-PAGE, transferred onto PVDF membranes, then subjected to western blot analysis. The membrane were labelled with fluorescent secondary antibody and analysed with a LICOR-Odyssey apparatus using IMAGE STUDIO Lite software, which enables quantitative analysis of blotting signals.

Immunoprecipitation

HeLa cells were treated as described in Figure legends and lysed in lysis buffer (50 mM Hepes, 50 mM NaCl, 10% glycerol, 1% Triton X-100, 1.5 mM MgCl, 5 mM EGTA)) for 15 min on ice and pelleted for 10 min at 13.000 rpm. The supernatant was incubated with the LC3 antibody (ab192890-ABCAM) or control IgG antibodies (2729S Cell Signaling) (1:100) for 3 h and 2 h with Dynabeads Protein A (Novex-Lifechnologies). The immunoprecipitate was eluted by boiling the samples in Laemmli buffer for 5 min. EGFP-tagged proteins (DNM2-pEGFP and pEGFP-LC3) were pulled down using GFP-TRAP beads (ChromoTek) according to the manufacturer's protocol. Proteins were resolved by SDS-PAGE. Similarly was done for Myc-TRAP.

Immunofluorescence Microscopy

Cells grown on coverslips at 25% confluency were fixed in 4% paraformaldehyde for 5 minutes, then permeabilised with 0.1% Triton or methanol. 1% BSA in PBS was used for blocking and for primary and secondary antibody incubations. The experiments visualizing endogenous LC3 were fixed with methanol for 5 minutes at -20°C. A Zeiss LSM710 confocal microscope was used for fluorescent confocal analysis. All confocal images were taken with a 63× oil-immersion lens.

HaloTag-LC3

The HaloTag-LC3 autophagosome completion assay was performed as previously described by Takahashi et al (Takahashi et al., 2018). Briefly, HaloTag-LC3 expressing cells were transfected with HA-DNM2-WT or mutants for 20 h on Matek 35 mm dishes (MatTek, Ashland MA USA; P35G-1.0-14-C) and incubated in MAS buffer (220 mM mannitol, 70 mM sucrose, 10 mM KH2PO4, 5 mM MgCl2, 2 mM HEPES, 1 mM EGTA) containing Seahorse XF-PMP (Agilent-1025 04 100) (2–3 nM) and MIL (Promega-G100A) at 37°C for 15 min. Cells were then fixed in 4% PFA for 5 min, washed three times in PBS, and incubated with mouse anti-HA antibody (Biolegend- 901501) for 1 h at room temperature. The cells were then incubated by goat anti-mouse Alexa 647 antibody and MPL (Promega- G825A) for 30 min. Imaging was performed on an incubated Zeiss AxioObserver Z1 microscope with a LSM780 confocal attachment using a 63× 1.4 NA Plan Apochromat oil-immersion lens.

Aggregate Quantification

The httQ74-HA aggregation was detected by immunofluorescence (primary HA antibody). The proportion of transfected cells with aggregates was scored (approx. 500 cells per coverslip). Experiments were performed blinded and in triplicate in at least three independent experiments. Statistics for aggregation assays were calculated as odds ratios.

Live Cell Imaging

HeLa cells were seeded on MatTek Petri dishes (Mat Tek, Ashland, MA, USA) at a density of approximately 1.5×10^5 cells per dish. Cells were placed in HBSS with HEPES, after which they were imaged immediately at 37°C. Each frame was 4.2 seconds. Imaging

was performed on an incubated Zeiss AxioObserver Z1 microscope with a LSM780 confocal attachment using a 63× 1.4 NA Plan Apochromat oil-immersion lens.

Superresolution Microscopy

Samples were stained for conventional fluorescence microscopy and mounted on high-precision size 1.5 coverslips (Carl Zeiss Ltd, Cambridge). Coverslips were mounted with ProLong Gold anti-fade medium (Life Technologies, P36934), which was left to cure for 3 days at room temperature in order to produce samples with a consistent refractive index. Super-Resolution Structured Illumination Microscopy (SR-SIM) was performed using an Elyra PS1 instrument (Carl Zeiss Ltd). Samples were examined on the microscope using a 63x 1.4NA plan-apo Carl Zeiss objective lens and Immersol 518F (23°C) immersion oil. Image acquisition was carried out using ZEN 2012 Elyra edition software in which data sets were collected with 5 grating phases, 5 rotations and sufficient z positions spaced 110 nm apart to form an approximately 2 μm deep volume of raw SR-SIM data. Optimal grating frequencies were selected for each wavelength used. Structured Illumination post-processing was performed in ZEN using parameters determined by automated analysis of the datasets. Reconstructed images were then corrected for spherical and chromatic aberrations using channel alignment information, which was created using a 3D array of multi-spectral beads previously imaged with the same instrument settings. The average final image resolution was calculated to be 110 nm in x and y dimensions and 240 nm in the z dimension which represents a two-fold lateral and axial improvement in resolution compared to conventional microscopy.

Electron Microscopy

HeLa cells stably expressing DNM2-EGFP WT or R465W and Fibroblasts from a patient carrying the DNM2 R465W mutation (Buono et al., 2018; Trochet et al., 2018) or a unaffected control were then placed at 37°C in HBSS for 1 h and fixed in a mixture 2% Paraformaldehyde and 2% Glutaraldehyde in 0.1 M cacodylate buffer (pH 7.4) for 1 h at room temperature. The cells were then post-fixed in 1% Osmium Tetroxide in 0.1 M cacodylate buffer (pH 7.4) for 20 min and processed for standard Epon embedding. The sections were observed using a Philips CM100 or FEI Tecnai Spirit electron microscopes.

Immunogold Electron Microscopy

Immunogold on Cryosections

HeLa cells were transfected with pEGFP-DNM2-WT or R465W for 24 h and fixed with a mixture of 2% paraformaldehyde and 0.2% glutaraldehyde in phosphate buffer (pH 7.4) for 2 h, at room temperature. Cells were then prepared for ultrathin cryosectioning and immunogold-labelled, as previously described (Puri et al., 2013). Briefly, fixed cells were washed once in PBS/0.02 M glycine, after which cells were scraped in 12% gelatin in PBS and embedded in the same solution. The cell-gelatin was cut into 1 mm blocks, infiltrated with 2.3 M sucrose at 4°C overnight, mounted on aluminium pins and frozen in liquid nitrogen. Ultrathin cryosections were picked up in a mixture of 50% sucrose and 50% methylcellulose and incubated with primary antibodies (rabbit anti-GFP) followed by protein A gold (Utrecht)(Puri et al., 2013).

FerroFluid

Tf-enriched membrane isolation using Magnetic Microbeads (Ferrofluid) was performed as previously described (Puri et al., 2018a). Similar approach was used with anti ATG9A antibody (1963-Eurogentech).

FACS-Based Endocytosis Assays

Transferrin-endocytosis assay was performed as previously described (Peden et al., 2004). Briefly, the cells were incubated for different time points (5 min, 10 min, 15 min and 20 min) in presence of Tf–Alexa-Fluor-647. Cells were then washed for various times before fixation in 4% paraformaldehyde in PBS. Cell-associated Tf–Alexa-Fluor-647 was determined by FACS analysis using BD FACSCalibur flow cytometer (BD Biosciences) and FlowJo software (Tree Star Inc.).

Purification of Recombinant LC3

LC3 was purified as described (Yin et al., 2016) with some modifications. Briefly, LC3B was expressed using a pGEX-6p1 plasmid in E coli for 3 h at 37°C after induction with 1 mM IPTG. Cells were lysed in 50 mM Tris pH 7.4, 150 mM NaCl using a sonicator in the presence of proteases inhibitors and centrifugated at 40,000 rpm for 30 min at 4°C. The supernatant was incubated with glutathione-Sepharose 4B beads followed by extensive washes in lysis buffer. PreScission Protease (GE Healthcare, 27-0843-01) was added at 100 units/ml in a 2-bed volume of PreScission Buffer (50 mM Tris-HCl pH 7.5, 150 mM NaCl, 1 mM EDTA) freshly prepared with 1 mM DTT and cleavage was performed overnight at 4°C. Cleaved protein was eluted and stored at -80°C.

Protein Binding Assay

Binding of LC3B (purified from E.Coli) to DNM2 (Origene, TP323585) was performed by incubation of recombinant proteins at 25ºC for 1 h, followed by immunoprecipitation with rabbit anti-DNM2 antibody (ABCAM, ab65556-1:700) and processed for western blot analysis.

QUANTIFICATION AND STATISTICAL ANALYSIS

Image Analysis

Volocity software (PerkinElmer) was used for analysis and processing of confocal images. For co-localization analysis of confocal images, we used Manders' Coefficient. All experiments were repeated at least three times. The background was fixed for all within-experiment analyses. Volocity software was also used for the Z stack reconstruction; the images presented also include the isosurface rendering in which there is no transparency and colocalized pixels do not appear as yellow.

For analysis of SIM images, final visualisation and video production was performed in Volocity 6.3 Software using isosurface rendering of selected cropped regions of the datasets. Isosurface rendering was used to more clearly visualise the shapes of fluorescent structures within the complex fluorescence volume datasets. This rendering type produces a three-dimensional surface contour connecting points in space which have the same fluorescence intensity value (a threshold value), this value defines what is inside or outside of an object and allows us to visualise the point where the signal rises above background values. Structures rendered in this way appear solid and therefore what is inside or behind them is hidden from the viewer's perspective. It is not possible to directly observe colocalization of signals in such images, instead we simply visualise the contact and overlap of the object's shapes.

In all the experiments in which we quantified the percentage of cells with RAB11A tubules we analysed how many cells had RAB11A in tubulation states compared with the total. In panel 1A left hand panel we have 3 cells which we scored as having tubules, while the cells in the right hand panel of Figure 1A were not considered to have this tubulation state. We always analysed at least 250 cells in duplicate per experiment, in each condition, in three independent experiments. The quantification was done directly on the microscope with the identity of the slides blinded to the person doing the analysis.

Statistics

Significance levels for comparisons between two groups were determined with t test (2-tailed). *= $p \leq 0.05$; **= $p \leq 0.01$; ***= $p \leq 0.001$. A p value of 0.05 was considered as the borderline for statistical significance.

For experiments where we have considered data from multiple independent experiments, we have normalised control data and used 1-sample t tests. For LC3-II blots, we have normalised both basal and bafilomycin A1 data.

For some experiments where we have assessed colocalizations in different conditions or western blot analysis, we have reported data from representative single experiments and noted cell numbers in the legends. This approach was used to minimise effects of heterogeneity between experiments.

Excel and Prism 7 software were used for statistical analysis and generation of graphs. See details in the figure legends.